JOURNAL OF COMPUTATIONAL PHYSICS 113, 82–111 (1994)

A Wavelet Monte Carlo Method for Turbulent Diffusion with Many Spatial Scales

FRANK W. ELLIOTT, JR.*

Program in Applied and Computational Mathematics, Princeton University, Princeton, New Jersey 08544

AND

ANDREW J. MAJDA†

Department of Mathematics and Program in Applied and Computational Mathematics, Princeton University, Princeton, New Jersey 08544

Received September 24, 1993

A new algorithm is developed here for Monte Carlo simulation of turbulent diffusion with random velocity fields having a power law spatial spectrum, arbitrarily many statistical scales, long range correlations, and infrared divergence. This algorithm uses an expansion of the moving average representation of a Gaussian random field via a specific orthonormal basis which exploits the scaling behavior of the random field and yields a compact representation of the field despite infrared divergence. The orthonormal basis involves a family of wavelets due to Alpert and Rokhlin and the vanishing of a large number of moments for this basis (order 3 or 4) is crucial for compact representation of the statistical velocity field. The authors also develop a rigorous practical a priori energy criterion for truncation of the wavelet expansion; furthermore, for moment cancellations with orders 3 or 4 and a fixed energy tolerance, the number of Gaussian random basis elements needed by the method is sublinear in the exponent m, where $1 < |x| < 2^m$ denotes the range of active velocity scales. The algorithm developed here has remarkably low variance as regards sampling errors. For example, for the infrared divergent velocity spectrum corresponding to the Kolmogoroff spectrum in an exactly solvable model, the velocity structure function is simulated accurately for separation distances over more than five decades with only 792 random basis elements and 100 ensemble realizations; with this same singular spectrum in the model problem, the pair dispersion statistic for the passive scalar can be determined within errors of 3% throughout over five decades of pair separation distance with only 792 random elements, 1000 realizations, and a few hours calculation on a workstation. All of the computational algorithms and results are presented for a nontrivial exactly solvable model and are described within a mathematical framework of error analysis where analytic, sampling, and discretization errors are treated separately.

* Research Supported by Grant DARPA N00014-92-J-1796.

† Research Partially Supported by Grants ARO DAAL03-92-G-0010, DARPA N00014-92-J-1796, ONR N00014-89-J-1044,P00003, and NSF DMS-99301094.

INTRODUCTION

Here we develop a new Monte Carlo method for simulation of the detailed statistical behavior of a scalar quantity, T, which satisfies the advection equation

$$\frac{\partial T}{\partial t} + v \cdot \nabla T = 0 \tag{1.1}$$

with $v(x, t)$, an incompressible velocity field. The numerical methods developed here are specifically adapted to the challenging problems involving a random velocity field with

(a) a power law spatial spectrum and

(b) arbitrarily many statistical scales with long range velocity correlations including infrared divergence (see Section 2). (1.2)

Practical applications where the situation in (1.2) is satisfied for the passive scalar problem in (1.1) include predicting the statistics of markers in high Reynolds number turbulence [1, 2], the tracking of pollutants in the atmosphere [3], and the diffusion of tracers in heterogeneous porous media [4]. Besides experimental measurements for the statistics of the scalar, $T(x, t)$, there is a large theoretical effort in the physics and applied mathematics communities to predict the statistical behavior of $T(x, t)$ under the circumstances in (1.2). These theoretical predictions proceed through formal renormalized perturbation theories involving either physical space or Fourier space representation with partial summation of divergent perturbation series according to various recipes (see the Refs. in [1, 2, 5]).

0021-9991/94 $6.00

Statistical quantities for $T(x, t)$ that are of physical interest include the mean concentration, $\langle T(x, t)\rangle$, and the second order correlations, $\langle T(x, t)\, T(x', t')\rangle$, which are directly related to the relative diffusion of pairs of particles, the pair distance function (see Section 2 below and Chapter 8 of [1]). Here and below, the bracket $\langle Q\rangle$ is used to denote the statistical ensemble average of a quantity Q over suitable random velocity statistics. There is a great need for new reliable Monte Carlo methods to bridge the gap between theory and experiments for statistical predictions for $T(x, t)$ when the velocity field has arbitrarily many spatial scales with the behavior in (1.2).

Recently, Avellaneda and one of the authors ([5–9]) have developed a mathematically rigorous exact analysis of several statistical issues for (1.1) with velocity fields satisfying (1.2) in a class of models involving simple shear layers with many spatio-temporal scales which, despite their simplicity, capture a number of interesting phenomena from the more complex general problems in (1.1), (1.2). Even more recently, Horntrop and one of the authors [10] have developed the explicit exactly solvable statistical theory for the special case of the shear layer models given by

$$\frac{\partial T}{\partial t}+\bar{w}\frac{\partial T}{\partial x}+v(x)\frac{\partial T}{\partial y}=0, \tag{1.3}$$

where $\bar{w}$ is a constant representing the effect of large scale mean flow. The random shearing velocity, $v(x)$, in (1.3) is a stationary Gausisian random field with zero mean, i.e., $\langle v\rangle=0$, and is completely characterized by the two-point correlation function

$$\begin{aligned} R(x) &= \langle v(x+x')\, v(x')\rangle \\ &= \int e^{2\pi i x k}\, E(k)\, dk \end{aligned} \tag{1.4}$$

with $E(k)$ the real valued energy density satisfying $E(-k)=E(k)$. With suitable choices for the energy density, $E(k)$, the statistical behavior in (1.2) can be achieved and analyzed explicitly (see [10] and Section 2 below). The exact formulas and subtle new statistical features for the simple model in (1.3) which have been documented in Ref. [10] provide an important class of elementary test problems for Monte Carlo methods for (1.1), (1.2) with an unambiguous theoretical basis; Ref. [11] contains a discussion and analysis of the capability of existing Monte Carlo methods to reproduce the statistical features of the model in (1.3).

Here we present the new Monte Carlo procedure in the context of the unambiguous exactly solvable model in (1.3). There is a direct and immediate application of these numerical algorithms to new mathematically rigorous random shearing direction models for isotropic turbulent diffusion satisfying (1.1) and (1.2) which have recently been developed by one of the authors [12]; this application will be reported elsewhere [13]. In the remainder of this introduction, we outline the salient features of the new algorithm and also provide a brief summary of the contents of the remainder of this paper.

In Section 2 we summarize the exact formulas and scaling behavior established in Ref. [10] regarding the statistical theory for the model in (1.3) as necessary background. Section 3 contains the conceptual development of the statistical method for the velocity field, $v(x)$, which involves four main steps:

(1) Use of a generalized moving average representation [14, 15] for a stationary power law Gaussian random field with infrared divergences;

(2) expansion of the moving average representation from Step (1) via an orthonormal basis of functions;

(3) judicious choice of an explicit orthonormal basis which respects scaling laws for singular power law spectra with economy of representation;

(4) a rigorous energy criterion for accurate compact truncation of the basic representation. (1.5)

While steps (1) and (2) are general and straightforward, the success of the Monte Carlo method developed in this paper as a practical algorithm depends crucially on steps (3) and (4). Here we utilize as an orthonormal basis a specific "wavelet" basis constructed by Alpert and Rokhlin [16–18] with the form

$$\phi_{mn}^{\sigma\tau}(x)=2^{m/2}\phi^{\sigma\tau}(2^m x-n), \tag{1.6}$$

where m and n are arbitrary integers. Here τ defines the order of the method and for each τ, the functions $\phi^{\sigma\tau}$, $\sigma=1, \ldots, \tau$, are a fixed finite number of piecewise polynomial functions with support on (0, 1) which satisfy the *moment cancellation conditions:*

$$\int_0^1 \phi^{\sigma\tau}(x)\, x^q\, dx=0, \qquad q=0, 1, \ldots, \tau-1. \tag{1.7}$$

With this piecewise polynomial basis, despite the infrared divergence, we are able to exploit the scaling properties of a power law random field as well as the scaling properties inherent in (1.6) to develop mathematically rigorous explicit infinite series for the random field $v(x)$ involving sums of independent Gaussian random variables.

In Section 3 we also develop a rigorous energy criterion which allows us to truncate the infinite series in a very compact fashion provided the order τ is large enough by exploiting suitable far field decay estimates implied by (1.7). With the infrared divergence in the velocity spectrum studied here, energy tolerances of 10^{-9} are typically needed; for a random field $v(x)$ with active scales ranging from $1 < |x| < 2^{30}$ only 792 Gaussian random basis elements are needed to achieve this tolerance with the method of order $\tau = 4$. On the other hand, the value $\tau = 1$ yields the classical Haar wavelet and for the smaller number of active velocity scales ranging from $1 < |x| < 2^{20}$ more than 10^5 Gaussian random basis elements are needed for the lower energy tolerance of order 10^{-6} so this classical choice is not practical. In fact for $\tau = 3, 4$, we document in Section 3 that for the Kolmogoroff spectrum in the model with a fixed energy tolerance, the *number of Gaussian random basis elements needed by the method is sublinear in the exponent m where* $1 < x < 2^m$ *denotes the range of active velocity scales.* It is worth remarking here that the large moment cancellation in (1.7) for $\tau = 3, 4$ is crucial to the success of our methods but the smoothness properties of general wavelets ([19]) are not needed; the Alpert–Rokhlin multiwavelets have precisely these features, together with explicit formulas which allow for rigorous a priori energy criteria for practical truncation for velocity fields with infrared divergent spectra. Some mathematical details from Section 3 are relegated to the Appendix.

In Section 4 we develop several practical details regarding the implementation of the random field algorithm from Section 3. Straightforward storage of the 792 Gaussian random fields required for velocity scales with a range $1 < |x| < 2^{30}$ would be prohibitive for most calculations on a workstation. We present an economical recursive scheme for generating the random weights which requires minimal storage. In fact, if P evaluations are needed, then the total number of weights evaluated by this scheme is no more than $O(PM)$ where the velocity field has 2^M active scales. These alternative algorithms compare favorably as regards random field evaluation with other recent schemes for generating power law random fields [20] and should be useful in other contexts.

In Section 5 we report on the performance of the wavelet Monte Carlo method for the model problem in (1.3) with an infrared divergent spectrum corresponding to the Kolmogoroff value in the model [5–7]. *We are able to simulate the velocity structure function accurately for over five decades with only 792 random elements and 100 ensemble realizations!!* Thus, the method has remarkably low variance as regards sampling errors. In fact, we demonstrate in Section 5 that with this singular velocity spectrum the entire *pair dispersion statistic for the model with* $\bar{w} \neq 0$ *can be determined within errors of roughly* 3% *throughout five decades of pair separation distance with* 1000 *realizations and only* 792 *random elements* through a few hours of calculation on a workstation. In Section 5 we also explore the practical issue of the choice of a time step and determine a practical time step criterion for a given separation distance. All of our computational results in Section 5 are also described within a framework of error analysis where analytic, sampling, and discretization errors are treated separately. The less sensitive behavior of the mean square displacement is also discussed in a similar fashion in Section 5.

Various alternative Fourier series [15], spectral [21–23], and moving average representations [24] for random velocity fields have been developed specifically to study turbulent diffusion. The methods in Refs. [15, 21, 24] give good results with varying quality for band-limited spectra but are not suitable for velocity fields with long range correlations (see Ref. [11]). The randomization algorithms from Refs. [22, 23] have been reported in [23] to yield one decade of scaling for the pair dispersion in isotropic turbulent diffusion. The performance of all of these algorithms on the simple model problem in (1.3) for a wide variety of short-range and long-range correlated spectra is presented in Ref. [11]. The special version of the algorithms developed here involving Haar wavelets ($\tau = 1$) has been used earlier to study mean square displacements for tracers in porous media [25].

2. SCALAR STATISTICS IN THE EXACTLY SOLVABLE MODEL

Here we summarize various exact solutions, which we utilize in subsequent sections, for the statistical behavior of the scalar, $T(x, t)$, that satisfies the model problem,

$$\frac{\partial T}{\partial t} + \bar{w}\frac{\partial T}{\partial x} + v(x)\frac{\partial T}{\partial y} = 0. \tag{2.1}$$

The detailed calculations as well as other explicit facets of this model including, for example, the effects of finite molecular diffusion are contained in Ref. [10]. For simplicity in exposition, we restrict our attention in this paper to the most difficult situations with power law spectra, long range correlations, and infrared divergence. Other power law spectra will be treated elsewhere by the methods of this paper. Thus, the spectral energy function, $E(k)$, defined in (1.4) for the stationary Gaussian random field, $v(x)$, satisfies

$$E(k) = |k|^{1-\varepsilon}, \qquad 2 < \varepsilon < 4. \tag{2.2}$$

Here ε with $2 < \varepsilon < 4$ is a parameter; we emphasize the value, $\varepsilon = \frac{8}{3}$, throughout this paper because this value is analogous in the model problem of the Kolmogoroff $-\frac{5}{3}$ spectrum from turbulence theory [5–9]. Actually, because of the infrared divergence, there is only a suitable generalized

Gaussian random field, $v(x)$, with the energy spectrum in (2.2) (see Section 3 and Appendix A). Instead one needs to consider (see [5–10]) a zero mean Gaussian random field, $v^\delta(x)$, characterized by the two-point correlation function

$$R^\delta(x) = \langle v^\delta(x+x')\, v^\delta(x')\rangle = \int_{\delta<|k|} e^{2\pi i x\cdot k}\, |k|^{1-\varepsilon}\, dk, \qquad 2<\varepsilon<4, \quad (2.3)$$

and compute the limiting statistical behavior of the scalar $T(x, t)$ as $\delta \to 0$; this is subtle because there is infrared divergence of energy in the limit since

$$R^\delta(0) \to \infty \qquad \text{as} \quad \delta \to 0, \quad 2<\varepsilon<4. \quad (2.4)$$

In the model problem δ corresponds to a negative power of the Reynolds number in turbulence theory [6] and the behavior in (2.4) for $\varepsilon = \frac{8}{3}$ corresponds to the infrared divergence of energy in the high Reynolds number limit. Below we report on exact solution formulas for the scalar statistics [10] which incorporate this passage to the limit for the model problem in (2.1) despite this infrared divergence.

(2A) The Pair Distance Function and Pair Dispersion

The pair distance function, $P(t, x, y, x_0, y_0)$, is essentially the second-order correlation function of the scalar, T, and is a fundamental statistical quantity for turbulent flow [1, 2] since Richardson's pioneering work [26]. Next we describe this quantity for the shear layer models in (2.1). Consider two particles denoted by subscripts 1 and 2. Let particle 1 be located at (0, 0) at time $t=0$ while particle 2 is at (x_0, y_0) for $t=0$. Denote the particle trajectories in the x-direction by $X_j(t)$ and in the y-direction by $Y_j(t)$ for $j=1, 2$. For the simple shear layer model in (2.1), $X_j(t) = \bar{w}t + X_j(0)$ and $Y_j(t) = \int_0^t v(X_j(s))\, ds + Y_j(0)$. The pair distance function is defined as

$$P(t, x, y, x_0, y_0) = \text{Prob}\{X_2(t) - X_1(t) = x,\ Y_2(t) - Y_1(t) = y \mid X_2(0) - X_1(0) = x_0,\ Y_2(0) - Y_1(0) = y_0\}. \quad (2.5)$$

Despite the infrared divergence in (2.4), an explicit closed evolution equation for the pair distance function for the model with the velocity spectrum in (2.2) is derived in Ref. [10]. This evolution equation has the form

$$\frac{\partial P}{\partial t} = D(t, x, \bar{w})\, \frac{\partial^2 P}{\partial y^2} \quad (2.6)$$

with remarkable sensitive dependence on the mean flow, $\bar{w}$, for $\bar{w} \neq 0$ (see [10]). An important statistical measurement calculated from the pair distance function is the mean square dispersion which is directly related to the size of clouds [1, 2, 26]. For the simple models in (2.1), only the y-component of the mean square dispersion, $\langle l_y^2\rangle$, is non-trivial and it is defined by

$$\langle l_y^2\rangle = \int y^2 P(t, x, y, x_0, y_0)\, dy. \quad (2.7)$$

Next we give explicit formulas for the mean square dispersion (see [10]). We introduce the constant

$$K_p = \int_{-\infty}^{\infty} (1 - \cos(2\pi k))\, |k|^p\, dk = -\frac{\pi^{-1/2-p}\Gamma(1/2 + p/2)}{\Gamma(-p/2)} \quad (2.8)$$

for $-3 < p < -1$. The *mean square dispersion* for $\bar{w} = 0$ in (2.1) is given explicitly by

$$\langle l_y^2\rangle(t, x) = \langle (v(0) - v(x))^2\rangle\, t^2 = 2K_{1-\varepsilon} x^{\varepsilon-2} t^2 \qquad \text{for} \quad 2<\varepsilon<4. \quad (2.9)$$

The *mean square dispersion* for $\bar{w} \neq 0$ in (2.1) is given explicitly by

$$\langle l_y^2\rangle(t, x) = \frac{4K_{1-\varepsilon}}{\varepsilon(\varepsilon-1)}\, |\bar{w}|^{\varepsilon-2} \times \left(|t|^\varepsilon + \left|\frac{x}{\bar{w}}\right|^\varepsilon - \frac{1}{2}\left|\frac{x}{\bar{w}} - t\right|^\varepsilon - \frac{1}{2}\left|\frac{x}{\bar{w}} + t\right|^\varepsilon \right), \quad (2.10)$$

for $2<\varepsilon<4$. With the simple form for the particle trajectories described above (2.5), we have $x = x_0$ in (2.5) so that x in both (2.9) and (2.10) corresponds exactly to the initial pair separation distance; also, the formulas in (2.9) and (2.10) are presented for the special case with $y_0 = 0$ in (2.5)—the general case involves adding the trivial term y_0^2 to the right-hand side of (2.9) and (2.10).

Both of the formulas in (2.9) and (2.10) satisfy the scaling laws, for $\lambda > 0$,

$$\langle l_y^2\rangle(\lambda t, \lambda x) = \lambda^\varepsilon \langle l_y^2\rangle(x, t). \quad (2.11)$$

This is verified immediately from (2.9) and (2.10) and is a direct consequence of the universal renormalization theory developed in Ref. [10] for the model in (2.1). In Section 5 we utilize this universal scale invariance from (2.11) to devise a class of stringent numerical tests for the Monte Carlo algorithm developed in this paper.

In Section 5 we utilize several analytic expressions for the *incremental covariance* of the Gaussian random field with the spectrum in (2.2). This statistical quantity is defined by

$$R(r, s) = \langle (v(r) - v(0))(v(s) - v(0)) \rangle$$
$$= \int_{-\infty}^{\infty} (e^{2\pi ikr} - 1)\overline{(e^{2\pi iks} - 1)}\, E(k)\, dk. \quad (2.12)$$

With the energy spectra in (2.2), we calculate that

$$R(r, s) = K_{1-\varepsilon}(|r|^{\varepsilon-2} + |s|^{\varepsilon-2} - |r-s|^{\varepsilon-2}) \quad \text{for} \quad 2 < \varepsilon < 4. \quad (2.13)$$

It is worth mentioning here that the *velocity structure function* given by $\langle (v(0) - v(x))^2 \rangle$ satisfies

$$\langle (v(0) - v(x))^2 \rangle = R(x, x) \quad (2.14)$$

and for the simple model in (2.1), this velocity structure function governs the behavior of the mean square dispersion for $\bar{w} = 0$ (see (2.9)).

(2B) Mean Statistics and Mean Square Displacements

The large-scale, long-time renormalized behavior of the mean statistics, $\langle T \rangle(t, x, y)$, for the model problem was studied in Refs. [6, 7] and a closed evolution equation for the mean statistics, analogous to (2.6) and valid for all times, was derived in Ref. [10]. Unlike the second-order statistics described earlier in (2.9) and (2.10), the mean statistics, $\langle T \rangle$, exhibit subtle effects of the infrared cutoff parameter δ defined in (2.3) in the limit as $\delta \to 0$ for the regime of ε with $2 < \varepsilon < 4$ (see [6, 7, 9], and Section 5 of [10]).

The most interesting functional of $\langle T \rangle$ which measures the mixing length is *mean square displacement*, $\langle Y^2(t) \rangle$, in the y-direction for (2.1) which is defined by

$$\langle Y^2(t) \rangle = \int y^2 \langle T \rangle\, dy \quad (2.15)$$

with point-source initial data for $\langle T \rangle$. Let $\langle Y_\delta^2(t) \rangle$ denote the mean square displacement for the problem in (2.1) with the subscript emphasizing dependence on the cutoff parameter. The rigorous theory from Refs. [6, 7] applies both for $\bar{w} = 0$ and $\bar{w} \neq 0$ and yields the universal behavior that as $\delta \to 0$,

$$\lim_{\delta \to 0} \frac{\langle Y_\delta^2(t) \rangle}{\bar{R}_\delta t^2} = 1 \quad (2.16)$$

for any fixed $t > 0$. Here the constant $\bar{R}_\delta$ is associated with the rescaled energy from (2.3) and is given by

$$\bar{R}_\delta = 4 \int_\delta^\infty |k|^{1-\varepsilon}\, dk = 4(\varepsilon - 2)^{-1} \delta^{2-\varepsilon}. \quad (2.17)$$

An explicit quantitative confirmation of the theoretical behavior predicted in (2.16) in the interesting situation with $\bar{w} \neq 0$ is presented in Section 5 of Ref. [10]. In Section 5 of this paper, we utilize the rigorous theoretical prediction in (2.16) as another stringent numerical test for the Monte Carlo method developed in this paper with the infrared divergent velocity spectra in (2.2).

3. DESIGN OF THE BASIC ALGORITHM

Here we carry out in detail the four main steps outlined in (1.5) for the development of a Monte Carlo method for Gaussian random velocity fields with infrared divergent spectra.

(3A) The Generalized Moving Average Representation

Here we design a Monte Carlo method to simulate the Gaussian random velocity field with the spectral representation

$$v(x) = \int_{-\infty}^{\infty} e^{2\pi ikx} E^{1/2}(k)\, dW_k, \quad (3.1)$$

where

$$E(k) = |k|^{1-\varepsilon} \quad \text{for} \quad 2 < \varepsilon < 4 \quad (3.2)$$

is the infrared divergent spectrum of the random field and W is standard Brownian motion. (We consider the essential properties of such stochastic integrals with respect to Brownian motion in Appendix A.) Because our goal is to simulate the particle trajectories for (2.1), we represent $v(\cdot)$ in physical space. We will develop our method from the *moving average representation* (see [14, 15]),

$$v(x) = \int_{-\infty}^{\infty} \left(\int_{-\infty}^{\infty} E^{1/2}(k)\, e^{-2\pi ik(x-y)}\, dk \right) dW_y$$
$$= \int_{-\infty}^{\infty} G(x - y)\, dW_y, \quad (3.3)$$

by localizing the dependence of $v(x)$ on W. Here G is the inverse Fourier transform of the square root of the spectrum in (3.2) and has the formula

$$G(x) = (\mathscr{F}^{-1} E^{1/2})(x)$$
$$= K |x|^\lambda, \quad (3.4a)$$

where

$$K = \frac{\pi^{-(1+\varepsilon/2)} \Gamma(1 + \varepsilon/2)}{\Gamma((\varepsilon - 1)/4)} \quad (3.4b)$$

and

$$\lambda = \frac{\varepsilon - 3}{2} \quad \text{for} \quad 2 < \varepsilon < 4. \quad (3.4c)$$

Here the Fourier transform is defined by

$$(\mathscr{F}f)(k) = \int_{-\infty}^{\infty} f(x)\, e^{2\pi i k x}\, dx,$$

and $\mathscr{F}^{-1}$ is the corresponding inverse Fourier transform. In contrast to the usual technique of simulating a moving average process by integration against a Brownian path, we use a multiscale orthonormal basis which is adapted to the kernel G so that the moving average integral can be computed rapidly and accurately.

The variance of the field at a point x is the integral of the spectrum, which is infinite for all values of ε with $2 < \varepsilon < 4$ for the spectrum in (3.2) due to the infrared divergence. Therefore, as in the theory of distributions, we consider only integrals of the field with respect to test functions so that the resulting stochastic integrals will be Gaussian random variables with zero mean and finite variance. We denote the integral of a test function f with respect to $v(\cdot)$ by $V(f)$ with $V(f)$ defined by

$$V(f) = \int_{-\infty}^{\infty} f(x)\, v(x)\, dx. \tag{3.5}$$

With the moving average representation for $v(x)$ in (3.3), we have the identities

$$V(f) = \int_{-\infty}^{\infty} (\mathscr{F}f)(k)\, E^{1/2}(k)\, dW_k \tag{3.6a}$$

and

$$V(f) = \int_{-\infty}^{\infty} (G * f)(x)\, dW_x. \tag{3.6b}$$

(Here and below we use equality for two random processes with the same finite-dimensional distributions.) The function $f*g$ is the convolution given by

$$(f*g)(x) = \int_{-\infty}^{\infty} f(x-y)\, g(y)\, dy.$$

With the formulas in (3.6a) and (3.6b), we can characterize exactly when a function f is an allowable test function for the generalized random field in (3.1). We need to require that $\langle |V(f)|^2 \rangle < \infty$ and from (3.6a), this condition means that

$$\langle |V(f)|^2 \rangle = \int_{-\infty}^{\infty} |(\mathscr{F}f))(k)|^2\, |k|^{1-\varepsilon}\, dk < \infty. \tag{3.7}$$

In particular, if f is a function with an analytic, square integrable or bounded Fourier transform which has a zero of order $n > \varepsilon/2 - 1$ at $k = 0$, then f is a valid test function for the generalized random field in (3.1) because the integral in (3.7) is finite. Important examples of allowable test functions for the numerical method developed here are given by functions $f(x)$, where f is piecewise polynomial with compact support and satisfies

$$\int_{-\infty}^{\infty} f(x)\, x^p\, dx = 0$$

for $0 \leqslant p < n$ with $n > \varepsilon/2 - 1$ for $2 < \varepsilon < 4$. For any two test functions f and g both representations of $V(\cdot)$ in (3.6a) and (3.6b) have the first and second moment properties

$$\langle V(f) \rangle = 0 \tag{3.8a}$$

$$\langle V(f)\, \overline{V(g)} \rangle = \int_{-\infty}^{\infty} (\mathscr{F}f)(k)\, \overline{(\mathscr{F}g)(k)}\, E(k)\, dk$$

$$= \int_{-\infty}^{\infty} (G * f)(x)\, \overline{(G * g)(x)}\, dx. \tag{3.8b}$$

(3B) An Orthonormal Expansion for the Moving Average Representation

We will derive our method from the moving average representation, formula (3.3) using the orthonormal expansion of white noise given in Appendix A. For any square integrable functions g and h on the real line, we use the notation

$$(g, h) = \int_{-\infty}^{\infty} g(x)\, \overline{h(x)}\, dx,$$

for *inner product* and define *white noise* as the linear map

$$N(g) = \int_{-\infty}^{\infty} g(x)\, dW_x,$$

which sends functions into Gaussian random variables (see Appendix A). Let $\{\phi_n | n = 0, 1, \ldots\}$ be an orthonormal basis for the square integrable functions on the real line. Any square integrable g has the expansion

$$g = \sum_{n=0}^{\infty} (g, \phi_n)\, \phi_n.$$

Therefore, as can be justified by formula (A.3) in Appendix A, this integral has the expansion

$$N(g) = \int_{-\infty}^{\infty} g(x)\, dW_x$$

$$= N\left(\sum_{n=0}^{\infty} (g, \phi_n)\, \phi_n \right)$$

$$= \sum_{n=0}^{\infty} (g, \phi_n)\, N(\phi_n).$$

For any allowable test function f, it follows from Eqs. (3.6b) and (3.7) that $(G * f)$ for g in the above expansion so that $V(f)$ has the expansion

$$\begin{aligned} V(f) &= \int_{-\infty}^{\infty} (G * f)(x)\, dW_x \\ &= N(G * f) \\ &= \sum_{n=0}^{\infty} (G * f, \phi_n)\, N(\phi_n). \end{aligned}$$

As indicated in Appendix A, $\{N(\phi_n) \mid n = 0, 1, \ldots\}$ is a sequence of independent and identically distributed Gaussian random variables with mean 0 and variance 1. (The partial sums of this representation correspond to processes which converge in finite-dimensional distribution to $V(\cdot)$.) Since convolution is a symmetric operation and satisfies

$$(G * f, \phi_n) = (f, G * \phi_n),$$

we obtain

$$V(f) = \sum_{n=0}^{\infty} (f, G * \phi_n)\, N(\phi_n), \tag{3.9}$$

provided that each ϕ_n is an allowable test function. Equation (3.9) describes the theoretical representation that we use in the numerical procedure.

(3C) The Alpert–Rokhlin Multiwavelet Basis

We will now consider multiwavelet orthonormal bases for the expansion of white noise in formula (3.9). We will describe multiwavelets, show that the homogeneity of G makes them particularly suited to multiwavelet expansion, describe the Alpert–Rokhlin multiwavelets, and show that these multiwavelets are adapted to the representation of $V(\cdot)$ in (3.9).

A *multiwavelet* (a generalized wavelet) is a set of functions $\{\phi^{\sigma\tau} \mid \sigma = 1, 2, \ldots, \tau\}$ that has the property that its discrete translates and dilates

$$\{\phi_{mn}^{\sigma\tau}(x) = 2^{m/2}\phi^{\sigma\tau}(2^m x - n) \mid m, n \in Z,\ \sigma = 1, 2, \ldots, \tau\} \tag{3.10}$$

form an orthonormal basis for $L^2(R)$. We will use the term *wavelet* to refer to a function from a multiwavelet, although the term usually refers to a single function whose dilates and translates form a basis for $L^2(R)$. The double subscript notation

$$\phi_{mn}^{\sigma\tau}(x) = 2^{m/2}\phi^{\sigma\tau}(2^m x - n)$$

for dilation and translation is standard for multiwavelets. The superscript τ denotes the order of the multiwavelet basis (see the definition below). The first subscript is called the *octave* and the second subscript is called the *translate*; we wish to reserve the use of the term *scale* to avoid later confusion. In this notation, an L^2 function g has the expansion

$$g = \sum_{\sigma=1}^{\tau} \sum_{m,n \in Z} (g, \phi_{mn}^{\sigma\tau})\, \phi_{mn}^{\sigma\tau}.$$

Assuming that the multiwavelet basis consists of allowable test functions for the generalized random field $V(\cdot)$ by utilizing the formula in (3.9),

$$V(f) = \sum_{\sigma=1}^{\tau} \sum_{m,n \in Z} (f, G * \phi_{mn}^{\sigma\tau})\, N(\phi_{mn}^{\sigma\tau}). \tag{3.11}$$

One apparent numerical difficulty is the convolution of G with all dilates and translates of $\phi^{\sigma\tau}$. Recall from Eq. (3.4) that G is a homogeneous function of x. Thus, by simple rescalings, once $G * \phi^{\sigma\tau}$ is known, then $G * \phi_{mn}^{\sigma\tau}$ is known for all m and n according to the formula

$$(G * \phi_{mn}^{\sigma\tau})(x) = 2^{m(-1/2-\lambda)}(G * \phi^{\sigma\tau})(2^m x - n). \tag{3.12}$$

Therefore, only τ convolutions need be computed.

DEFINITION (The Alpert–Rokhlin multiwavelets; see [16–18]). An Alpert–Rokhlin multiwavelet is a set of piecewise polynomial functions $\{\phi^{\sigma\tau} \mid \sigma = 1, 2, \ldots, \tau\}$ with support contained in $[0, 1]$ with the properties

Orthonormality,

$$(\phi_{mn}^{\sigma\tau}, \phi_{m'n'}^{\sigma'\tau}) = \delta_{\sigma\sigma'}\delta_{mm'}\delta_{nn'} \tag{3.13a}$$

Moment cancellation,

$$\int_0^1 \sigma^{\sigma\tau}(x)\, x^q\, dx = 0 \quad \text{for } q = 0, \ldots, \tau - 1 \tag{3.13b}$$

(Anti-)symmetry

$$\phi^{\sigma\tau}(1 - x) = (-1)^{\sigma+\tau-1}\, \phi^{\sigma\tau}(x), \tag{3.13c}$$

where δ_{ij} is the Kronecker delta and such that the dilates and translates (3.10) form a basis for $L^2(R)$ for each natural number τ.

For every τ such a family can be constructed through an orthonormalization procedure (see [16–18]). The first four families can be constructed from the collection of polynomials,

$$\begin{aligned} p^{11}(x) &= 1 \\ p^{12}(x) &= -1 + 2x \\ p^{22}(x) &= -2 + 3x \end{aligned}$$

$$p^{13}(x) = 1 - 24x + 30x^2$$
$$p^{23}(x) = 3 - 16x + 15x^2$$
$$p^{33}(x) = 4 - 15 + 12x^2$$
$$p^{14}(x) = 1 + 4x - 30x^2 + 28x^3$$
$$p^{24}(x) = -4 + 105x - 300x^2 + 210x^3$$
$$p^{34}(x) = -5 + 48x - 105x^2 + 64x^3$$
$$p^{44}(x) = -16 + 105x - 192x^2 + 105x^3$$

on (0, 1) via symmetric and anti-symmetric extension to $(-1, 1)$. This results in families of piecewise polynomial functions on $(-1, 1)$ determined by the formula

$$f^{\sigma\tau}(x) = \begin{cases} \dfrac{(-1)^{\sigma+\tau-1}}{\sqrt{2}\,\|p^{\sigma\tau}\|} p^{\sigma\tau}(-x) & \text{if} \quad x \in (-1, 0) \\ \dfrac{1}{\sqrt{2}\,\|p^{\sigma\tau}\|} p^{\sigma\tau}(x) & \text{if} \quad x \in (0, 1) \\ 0 & \text{otherwise,} \end{cases}$$

where

$$\|g\|^2 = \int_0^1 |g(x)|^2\, dx.$$

Translation and contraction to the interval (0, 1) gives the formula

$$\phi^{\sigma\tau} = \sqrt{2} f^{\sigma\tau}(2x - 1)$$

for function number σ in multiwavelet family τ.

With the moment cancellation properties in (3.13b), it follows from our discussion below (3.7) that the Alpert–Rokhlin multiwavelets are allowable test functions for the generalized random field in (3.1). Thus, the expansion in (3.11) with coefficients from (3.12) is valid. For the special case $\tau = 1$, the function $\phi^{11} = h$ is the Haar wavelet,

$$h(x) = \begin{cases} -1 & \text{if} \quad x \in (0, \tfrac{1}{2}) \\ +1 & \text{if} \quad x \in (\tfrac{1}{2}, 1), \\ 0 & \text{otherwise} \end{cases} \tag{3.14}$$

which was the first wavelet discovered (see [19]). We shall see that because this wavelet cancels only one moment it is not adequate for the effective numerical representation of the velocity field, $v(\cdot)$.

(3D) Truncation of the Multiwavelet Expansion and the Energy Criterion

We must truncate the multiwavelet expansion, Eq. (3.11), to include only a finite number of wavelets so that we can use it for numerical simulation of $v(\cdot)$. We first limit the number of octaves in the expansion and, then, the number of wavelets at each octave. If we include M contiguous octaves in our simulation, it does not matter which M octaves we include; we can convert any M-octave expansion into any other by simple scaling. At a given octave, we shall see that the wavelets nearest x contribute the most to the statistical energy (variance) of the field. Therefore, we use the formulas for the truncation of the field,

$$v(x) = \sum_{\sigma=1}^{\tau} \sum_{m,n \in Z} (G * \phi_{mn}^{\sigma\tau})(x)\, N(\phi_{mn}^{\sigma\tau}) \tag{3.15a}$$
$$\simeq \sum_{\sigma=1}^{\tau} \sum_{m=0}^{M-1} \sum_{n \in Z} (G * \phi_{mn}^{\sigma\tau})(x)\, N(\phi_{mn}^{\sigma\tau}) \tag{3.15b}$$
$$\simeq \sum_{\sigma=1}^{\tau} \sum_{m=0}^{M-1} \sum_{|n - \lfloor 2^m x \rfloor| < r_m} (G * \phi_{mn}^{\sigma\tau})(x)\, N(\phi_{mn}^{\sigma\tau}), \tag{3.15c}$$

where r_m is the *bandwidth* of the expansion at the mth octave. With $|n - \lfloor 2^m x \rfloor|$ appearing in formula (3.15c), the notation $\lfloor s \rfloor$ refers to the largest integer less than or equal to s. Equation (3.15b) is the M-octave expansion; Eq. (3.15c) shows the truncation of the field at each octave according to the proximity of each wavelet to x. As the number of octaves in an expansion-like formula (3.15b) approaches infinity, the approximate field converges (in distribution) to $v(\cdot)$. As the bandwidth r_m tends to infinity at each octave m in Eq. (3.15c), the approximated field converges to the field described in (3.15b). Therefore, these are convergent approximations for simulating the generalized random field $v(\cdot)$. It is worth remarking here that (3.12) can be used in the final approximation from (3.15c), yielding

$$\sum_{\sigma=1}^{\tau} \sum_{m=0}^{M-1} \sum_{|n - \lfloor 2^m x \rfloor| < r_m} (G * \phi_{mn}^{\sigma\tau})(x)\, N(\phi_{mn}^{\sigma\tau})$$
$$= \sum_{\sigma=1}^{\tau} \sum_{m=0}^{M-1} \sum_{|n - \lfloor 2^m x \rfloor| < r_m} 2^{m(-1/2 - \lambda)} \times (G * \phi^{\sigma\tau})(2^m x - n)\, N(\phi_{mn}^{\sigma\tau}) \tag{3.16}$$

with $\lambda = (\varepsilon - 3)/2$ for $2 < \varepsilon < 4$.

The success of the proposed algorithm based on (3.16) depends critically on the following fact:

> For fixed m, the convolutions $(G * \phi^{\sigma\tau})(2^m x - n)$ decay rapidly with increasing n, provided that the number of vanishing moments, τ, in (3.13b) is large enough. (3.17)

The fact in (3.17) allows for compact and efficient representation of the random field, provided that τ is large enough; we show below and in Section 5 that the Alpert–Rokhlin multiwavelet with order $\tau = 4$ provides sufficient accuracy

with economy of representation to yield over five decades of accurate scaling behavior for the second-order statistics in the model problem described in Section 2.

Next we state some explicit a priori decay estimates for the convolutions $G * \phi^{\sigma\tau}$ which quantify the fact in (3.17); these estimates lead to a practical essentially sharp a priori bound on the statistical energy depending on ε and τ for the terms ignored in the truncation at a given octave in going from (3.15b) to (3.15c). We state these bounds only for the unit scale, $m = 0$, for simplicity, since trivial rescaling allows us to achieve similar bounds for any other octave. We apply these bounds to a practical energy criterion immediately after their statement; the interested reader can consult Appendix B for the proofs.

THEOREM *Provided that ε satisfies $2 < \varepsilon < 4$, the number of moments canceled, τ, satisfies $\tau \geqslant 1$ and x satisfies $|n - \lfloor x \rfloor| \geqslant 4$, the convolutions $G * \phi^{\sigma\tau}$ satisfy the decay estimate*

$$|(G * \phi^{\sigma\tau})(x - n)| \leqslant K\, |n - \lfloor x \rfloor|^{\lambda - \tau}, \tag{3.18}$$

where $\lambda = (\varepsilon - 3)/2$ and K is the absolute constant in (3.4b).

This theorem has the following immediate consequence:

COROLLARY (Energy criterion). *For $2 < \varepsilon < 4$ and given an Alpert–Rokhlin multiwavelet with order τ, the statistical energy (variance) at the unit scale from all translates at a distance greater than or equal to r from x and defined by*

$$E_r = \left\langle \left| \sum_{|n - \lfloor x \rfloor| \geqslant r} (G * \phi^{\sigma\tau})(x - n)\, N(\phi^{\sigma\tau}_{mn}) \right|^2 \right\rangle$$

$$= K^2 \sum_{|n - \lfloor x \rfloor| \geqslant r} \left(\int_{-\infty}^{\infty} |x - y|^{\lambda}\, \phi^{\sigma\tau}(y - n)\, dy \right)^2 \tag{3.19}$$

satisfies the estimate

$$E_r \leqslant 2K \frac{(r-1)^{2(\lambda - \tau) + 1}}{2(\tau - \lambda) - 1} \tag{3.20}$$

for $r \geqslant 4$, where $\lambda = (\varepsilon - 3)/2$. In particular this energy in the "tails" decreases rapidly for larger values of the order τ.

Since the Haar wavelet corresponds to $\tau = 1$, from the corollary the rate of decay of the energy in the tails is very slow with the rate $o(r^{-4/3})$ for the Kolmogoroff spectrum value, $\varepsilon = \frac{8}{3}$; we will see below that the Haar wavelets require impractically many elements per octave compared with the other Alpert–Rokhlin multiwavelets with larger values of τ.

The Practical Energy Criterion for Truncation

Our practical criterion for determining the truncation of multiwavelets at each octave is that the total fraction of energy lost in all computed octaves in going from Eq. (3.15b) to Eq. (3.1c) should be less than a prespecified tolerance, t_e. The statistical energy lost in a given octave was computed according to the theoretical estimate in the corollary and these contributions were summed over the given number of octaves to determine the total energy lost. Table I shows the results of some computations to determine how the order of the moment cancellation τ affected the number of wavelets required for a given tolerance. We began with a 20-octave truncation according to Eq. (3.15c) with $\varepsilon = \frac{8}{3}$. We used energy tolerances $t_e = 10^{-4}$, 10^{-6}, and 10^{-8} to produce truncations according to formula (3.15c) for multiwavelets with $\tau = 1, 2, 3,$ and 4. For the Haar wavelet, $\tau = 1$, with $t_e = 10^{-4}$, 5496 wavelets were required for the 20-octave expansion. For the same wavelet with $t_e \leqslant 10^{-6}$ more than 100,000 wavelets were required for the entire expansion so that this Haar wavelet could not be used with smaller energy tolerances. For the second multiwavelet, $\tau = 2$, the numbers of wavelets required for $t_e = 10^{-4}$, 10^{-6}, and 10^{-8} were 244, 752, and 2868, respectively. For the third multiwavelet, $\tau = 3$, the numbers of wavelets required for $t_e = 10^{-4}$, 10^{-6}, and 10^{-8} were 300, 342, and 660, respectively. For the fourth multiwavelet, $\tau = 4$, the numbers of wavelets required for $t_e = 10^{-4}$, 10^{-6}, and 10^{-8} were 400, 400, and 448, respectively. At an energy tolerance of 10^{-6} the Haar wavelet required at least 250 times as many wavelets for the truncated expansion as the fourth-order Alpert–Rokhlin multiwavelet.

Obviously, the Haar wavelet is inadequate for accurate expansion of the field with $\varepsilon = \frac{8}{3}$. Since the field $v(\cdot)$ has infinite energy and most of the interesting statistics we will

TABLE I

The Sensitivity of Wavelet Count to Energy Tolerance

Multiwavelet order	Number of octaves	Energy loss tolerance	Number of wavelets[a,b]
1	20	10^{-4}	5496
1	20	10^{-5}	29314
1	20	10^{-6}	$\geqslant$100000
2	20	10^{-4}	244
2	20	10^{-6}	752
2	20	10^{-8}	2868
3	20	10^{-4}	300
3	20	10^{-6}	342
3	20	10^{-8}	660
4	20	10^{-4}	400
4	20	10^{-6}	400
4	20	10^{-8}	448

[a] For the Haar wavelet with energy tolerances of 10^{-6} or less, more than 100,00 wavelets were required for the full expansion. Since these requirements are far from practical as well as difficult to calculae accurately, we do not report them.

[b] The sensitivity of the expansion to energy tolerance decreases with the multiwavelet order.

TABLE II

Increase of Wavelet Count with the Number of Octaves

Multiwavelet order	Number of octaves	Energy loss tolerance	Number of wavelets
2	15	10^{-8}	2266
2	20	10^{-8}	2368
2	25	10^{-8}	3374
2	30	10^{-8}	3788
3	15	10^{-8}	519
3	20	10^{-8}	660
3	25	10^{-8}	795
3	30	10^{-8}	918
4	15	10^{-8}	340
4	20	10^{-8}	448
4	25	10^{-8}	556
4	30	10^{-8}	664

compute will involve the difference in the values of v at two points (see Section 2 and Section 5), we choose to work with small tolerances to avoid dynamic range errors in our numerical calculations. We could not consider a tolerance greater than 10^{-6}; therefore, we had the option of selecting $\tau = 3$ or 4, which had the two smallest wavelet counts for this tolerance. We chose $\tau = 4$ and used strict energy tolerances ($< 10^{-8}$) for our computations in Section 5. While this combination produced excellent results, we did not err too far on the side of caution.

We also determined that, for a fixed energy tolerance, the number of wavelets in an expansion is apparently linear in the number of octaves, as Table II indicates. For $\tau = 4$, $t_e = 10^{-8}$, and $M = 15$, the expansion required 340 wavelets. For the same values of τ and t_e, with $M = 20$, 25, and 30 levels, 448, 556, and 664 wavelets, respectively, were required. This reflects a growth which is slightly less than linear in M, the number of octaves. This is a remarkably compact representation of this random field.

4. IMPLEMENTATION OF THE METHOD

Accurate and rapid computation of the truncated field

$$v_M(x) = \sum_{m=0}^{M-1} \sum_{|n - \lfloor 2^m x \rfloor| < r_m} \sum_{\sigma=1}^{\tau} 2^{m(-1/2-\lambda)} \times (G * \phi^{\sigma\tau})(x-n)\, N(\phi^{\sigma\tau}_{mn+\lfloor x \rfloor}) \tag{4.1}$$

determined in Section 3 requires special considerations. First, while the convolutions involved are exactly computable, the exact formulas are numerically unstable for far-field ($|n - \lfloor x \rfloor|$ large) computations; therefore, we use a combination of exact and asymptotic formulas. Second, the random weights for the field must be computed in a manner that takes advantage of the sparseness of the formula in (4.1). Moreover, the method should not require the storage of all random numbers used to generate $v(\cdot)$ because the storage may be limited, especially in massively parallel computations with one field realization per processor. Furthermore, since only a few random numbers are used in the computation of $v(x)$ for a given x, most of the numbers necessary to generate the entire field will never be used.

(4A) Computation of Convolutions

We will now describe how we precompute the convolutions of the kernel with the multiwavelet $\{\phi^{\sigma\tau} \mid \sigma = 1, \ldots, \tau\}$; these convolutions are stored as functions of x for rapid evaluation during the simulation of the field $v(\cdot)$. As we have said, we use both exact formulas for x near $[0, 1]$ (the support of the multiwavelet) and asymptotic formulas for x far from $[0, 1]$. This precaution is necessary because the exact formulas are numerically unstable for x far from $[0, 1]$ and the asymptotic formulas will not converge for x in $[0, 1]$. The unit-scale multiwavelet $\{\phi^{\sigma\tau} \mid \sigma = 1, \ldots, \tau\}$ is composed of functions which are piecewise polynomial on $[0, 1]$. Therefore, we can exactly compute the convolution $(G * \phi^{\sigma\tau})(x)$, for $G(x) = K|x|^\lambda$, by computing integrals of the form

$$\int_a^b K|x-y|^\lambda p(y)\,dy = \begin{cases} \displaystyle\int_x^b K(y-x)^\lambda p(y)\,dy - \int_x^a K(y-x)^\lambda p(y)\,dy & \text{if } x < a < b \\ \displaystyle\int_a^x K(x-y)^\lambda p(y)\,dy + \int_x^b K(y-x)^\lambda p(y)\,dy & \text{if } a < x < b \\ \displaystyle\int_a^x K(x-y)^\lambda p(y)\,dy - \int_b^x K(x-y)^\lambda p(y)\,dy & \text{if } a < b < x. \end{cases} \tag{4.2}$$

For x near $[0, 1]$, the exact formula for $(G * \phi^{\sigma\tau})(x)$ is numerically accurate. For x far from $[0, 1]$, this formula involves the difference of two nearly equal quantities so that it cannot be computed accurately with limited precision arithmetic. Therefore, we limited the use of the exact formula to $-\frac{1}{2} \leqslant x \leqslant \frac{3}{2}$.

For x more than a distance $\frac{1}{2}$ from $[0, 1]$, we computed the convolution using the asymptotic formula that we derived through binomial expansion of $|x-y|^\lambda$,

$$(G * \phi^{\sigma\tau})(x) = \begin{cases} K \sum_{q=0}^{q_1} C(\lambda, q)(-1)^q M_q^{\sigma}(x)^{\lambda - q}, \\ \quad x > 1 \\ K(-1)^{\tau+\sigma} \sum_{q=0}^{q_1} C(\lambda, q)(-1)^q \\ \quad \times M_q^{\sigma}(1-x)^{\lambda-q}, \qquad x < 0, \end{cases} \tag{4.3}$$

where $C(\lambda, q)$ is the binomial coefficient and

$$M_q^{\sigma} = \int_0^1 x^q \phi^{\sigma\tau}(x)\, dx$$

is the qth moment of $\phi^{\sigma\tau}$. As $q_1 \to \infty$, this series converges absolutely; by ensuring that x is a prescribed distance from $[0, 1]$, we controlled the rate of convergence to minimize the degree of the polynomial used to compute the convolution to a given accuracy.

(4B) Computation of Random Weights

It is essential to compute the values of the random weights in the truncation formula (4.1) carefully because the total number of random weights that would be needed to simulate $v(x)$ for $x \in [0, 1]$ is exponential in M (about $2^M - 1 + 2bM$, where $b = \sup\{r_m \mid m = 0, 1, ..., M-1\}$ and r_m is the number of multiwavelets to the left or right of x at scale m), while the number of weights required to evaluate v at a single x is linear in M (about $M(2b+1)$). If P evaluations are needed, then the total number of weights evaluated is no more than $PM(2b+1)$. Since P is not a function of M, selective computing of the weights reduces the amount of work required from an exponential quantity to a linear quantity. Therefore, we will describe an efficient means for computing the random weights as needed, which results in such linear behavior. We begin by determining which weights are needed for a particular evaluation, we then use the algebra of random number generation to show how weights can be generated selectively, and, finally, we derive an efficient recursive scheme for generating these weights.

For $x \in [0, 1)$, the weights

$$w = \{N(\phi_{mn}^{\sigma\tau}) \mid m = 0, ..., M-1, \quad n = -b, ..., b + 2^m, \quad \sigma = 1, ..., \tau\} \tag{4.4}$$

where b is the maximum wavelet "radius" over all scales, may be required for the simulation of the field $v(\cdot)$ (see formula (4.1)). Because white noise $N(\cdot)$ preserves the orthonormality of the multiwavelet basis, these weights are independent and identically distributed standard normal random variables. However, for a given x, only those weights for wavelets near x,

$$w(x) = \{N(\phi_{mn}^{\sigma\tau}) \mid m = 0, ..., M-1, \quad |n - \lfloor 2^m x \rfloor| \leqslant r_m, \quad \sigma = 1, ..., \tau\}, \tag{4.5}$$

will be needed. Our implementation computes $w(x)$ as a subset of w recursively for a given seed u_0 and a given x by binary expansion of x.

We begin by associating with w a sequence $\{\gamma_p\}$ of i.i.d. standard normal random variables

$$N(\phi_{mn}^{\sigma\tau}) = \gamma_p, \tag{4.6a}$$

where

$$p = (2^m + n + 2mb + b - 1)\,\tau + \sigma - 1. \tag{4.6b}$$

This association orders w from scale 0 to scale $M-1$ and from left to right.

The sequence $\{\gamma_p\}$ is simulated from a transformation of $\{u_p \mid p = 0, 1, ..., c-1\}$, a finite sequence of random variables which are uniform on $\{0, 1, ..., c-1\}$, where $c = 2^{32}$. The Box–Muller transformation, which maps $\{u_p\}$ to $\{\gamma_p\}$, is

$$\gamma_p = \begin{cases} (-2\ln(u_p/c))^{1/2} \cos(2\pi u_{p+1}/c), & \text{if } p \text{ is even,} \\ (-2\ln(u_{p-1}/c))^{1/2} \sin(2\pi u_p/c), & \text{if } p \text{ is odd.} \end{cases} \tag{4.7}$$

Since u_{p+1} and u_{p-1} can both be obtained from u_p, we consider γ_p to be a function of u_p.

The sequence $\{u_p\}$ is defined by the recurrence relation $u_p = f(u_{p-1}) = au_{p-1} + b \pmod c$. The set $w(x)$ consists of M continguous blocks (one per scale) of $(2b+1)\tau$ numbers from $\{\gamma_p\}$ which is generated from $\{u_p\}$. We require a way of jumping over the very large irrelevant portions of $\{u_p\}$ to access the relevant portions. Fortunately, the algebraic properties of f provide a technique for jumping forwards and backwards in $\{u_p\}$. The function f is a linear congruential generator (lcg); a is relatively prime with respect to c so that f is reversible. The collection of reversible lcgs forms a group under composition so that if

$$f_1(x) = a_1 x + b_1 \pmod c \tag{4.8a}$$

and

$$f_2(x) = a_2 x + b_2 \pmod c, \tag{4.8b}$$

then

$$(f_2 * f_1)(x) = a_2 a_1 x + a_2 b_1 + b_2 \pmod c. \tag{4.8c}$$

Moreover, f generates a group of maximum cycle length c so that $f^{c-1} = f^{-1}$. This enables us to jump within the sequence $\{u_p\}$ by using powers of f so that

$$u_{p+q} = f^q(u_p)$$

for a positive or negative integer q. The power f^q can be computed in time logarithmic in q so that this technique is far more rapid than iterating through the sequence.

We compute $w(x)$ one scale at a time. For the mth scale we compute the u_p associated with $N(\phi^{1\tau}_{m\lfloor x^m x\rfloor})$ (the weight of the "first" wavelet containing x at the mth scale) directly and use f and f^{-1} to move backward and forward in $\{u_p\}$ to determine the adjacent weights. The index $p(m, x)$ associated with the wavelet containing x at scale m is

$$p(m, x) = (2^m + \lfloor 2^m x \rfloor + 2mb + b - 1)\tau.$$

While we could compute $f^{p(m,x)}$ directly to compute $u_{p(m,x)}$, there is a simple recursive technique which is faster. The index $p(m, x)$ has the decomposition

$$\begin{aligned} p(m, x) &= p_2(m, x) + p_1(m) + (b-1)\tau \\ p_2(m, x) &= (2^m + \lfloor 2^m x \rfloor)\tau \\ p_1(m, x) &= 2mb\tau. \end{aligned}$$

(The index $p_2(m, x)$ determines the number of the dyadic interval at scale m contaning x, and the rest of $p(m, x)$ is bookkeeping for weights for wavelets at the boundary of $[0, 1]$.) We can also define the corresponding powers of f as functions of m and x by $f^{p(m,x)} = F(m, x)$, $f^{p_1(m,x)} = F_1(m, x)$, and $f^{p_2(m,x)} = F_2(m, x)$. They obey the recurrence relations

$$\begin{aligned} x_0 &= x + 1 \\ F_1(0) &= 0 \\ F_2(0, x) &= \tau \\ x_m &= 2x_{m-1} \\ F_1(m, x) &= F_1(m-1, x) * f^{2b\tau} \\ F_2(m, x) &= F_2(m-1, x)^2 * f^{(\lfloor x_m \rfloor \bmod 2)\tau} \\ F(m, x) &= F_2(m, x) * F_1(m) * f^{(b-1)\tau}, \end{aligned} \tag{4.9}$$

where $M - 1 \geqslant m > 0$. Since $(\lfloor x_m \rfloor \bmod 2)\tau$ is 0 or τ, all explicit powers of f in these recurrence relations can be precomputed; no more than five products of lcgs need be computed for each jump in $w(x)$ with this method. Direct computation of $f^{p(m,x)}$ could require as many as $2m$ products of lcgs.

Our technique for random weight generation for the field (formula (4.1)) makes massively parallel implementation by our method trivial. This method requires no storage for $\{\gamma_p\}$, which would require 32 Mbytes per realization for a field with 20 octaves (i.e., $M = 10$). With 1000 realizations running simultaneously the total storage requirements for $\{\gamma_p\}$ would be about 32 Gbytes, which is clearly prohibitive. Furthermore, using the power method we can simultaneously initialize several approximately independent realizations of the field and run them independently on a single instruction multiple data (SIMD) multiprocessor machine.

5. COMPUTATIONAL RESULTS FOR THE MODEL PROBLEM

Here we apply the wavelet Monte Carlo algorithm developed in Sections 3 and 4 to the computation of scalar statistics for the model problem for turbulent diffusion summarized in Section 2 (see (2.1), (2.2)). Thus, the Gaussian random velocity field, $v(x)$, from (3.1) with the infrared divergent spectrum in (3.2) is simulated by the approximation

$$\begin{aligned} v(x) \simeq \sum_{\sigma=1}^{\tau} \sum_{m=0}^{M-1} \sum_{|n - \lfloor 2^m x \rfloor| < r_m} & 2^{m(-1/2-\lambda)} \\ & \times (G * \phi^{\sigma\tau})(2^m x - n)\, N(\phi^{\sigma\tau}_{mn}) \end{aligned} \tag{5.1}$$

with $G(x) = K|x|^\lambda$ and $\lambda = (\varepsilon - 3)/2$ for $2 < \varepsilon < 4$. In (5.1) $N(\phi^{\sigma\tau}_{mn})$ are independent Gaussian random variables with mean 0 and variance 1. Motivated by our results in Section 3 based on the practical energy criterion, we use the value $\tau = 4$ for the order of the Alpert–Rokhlin multiwavelet basis with an energy tolerance of one part per billion, i.e., $t_e = 10^{-9}$, to determine the truncated wavelet expansion. In the calculations presented below, the number of octaves in the truncation ranges from $M = 20$ to $M = 25$ to $M = 30$. With this energy criterion, the 20-octave truncation had 560 wavelets, the 25-octave truncation had 676 wavelets, and the 30-octave truncation has 792 wavelets. We denote by v^M the M octave truncated field described in formula (5.1) with the bandwidth factors, r_m, for $m = 0, \ldots, M-1$ determined by the energy criterion from Section 3.

We present numerical results for statistics of the scalar, $T(x, t)$, satisfying the model problem in (2.1) for the parameter value, $\varepsilon = \frac{8}{3}$, which is the analogue of the Kolmogoroff spectrum in the model. We present computational results for the mean square (pair) dispersion of the scalar, $T(x, t)$, for over five decades of separation distance. These results are obtained by integrating the y-component of the particle trajectory equation with the velocity approximation from (5.1). We recall the explicit exact formulas for the mean square dispersion for the model problem for the case $\bar{w} = 0$ from (2.9) and for the case $\bar{w} \neq 0$ from (2.10). We see from (2.9) and (2.14) that the scalar pair dispersion for the simpler situation with $\bar{w} = 0$ essentially tests the capability of the Monte Carlo approximations from (5.1) to reproduce the velocity structure function over a wide range of scales. The more difficult case for the mean square dispersion with $\bar{w} \neq 0$ and exact formulas summarized in (2.10) is a more stringent test where we will

develop a useful time step criterion based on the separation distance.

We also exploit the self-similar scaling character of the exact pair dispersion statistics for both $\bar{w}=0$ and $\bar{w}\neq 0$ as expressed by the scaling law in (2.11) as a stringent numerical test. The Monte Carlo approximations based on (5.1) do not exactly satisfy these scaling laws but we calculate the range (over five decades), where a very accurate approximation (within 3%) to the scaling law in (2.11) is achieved. Thus, we often rescale the computed data for the pair dispersion as well as other statistical quantities in a fashion consistent with the scaling law in (2.11). We define the *dissipation length*, d_0, to be the length of the support of the smallest wavelet in the truncated expansion in (5.1), i.e., $d_0 = 2^{1-M}$. The data which we present below are often scaled by some factor d which is a small multiple of the dissipation length d_0 with the time t and the separation distance x scaled by d^{-1}. We scale the pair dispersion by the factor $d^{-\varepsilon}$ according to the exact theoretical formula in (2.11); with the formula in (2.13), we scale the incremental covariance defined in (2.12) by $d^{2-\varepsilon}$. While we mostly present numerical results for the much more difficult statistics of the scalar involving pair dispersion, we conclude this section by computing the mean square displacements in the model with the Monte Carlo algorithm based on the representation in (5.1). Here we compare the computed results with the rigorous theoretical prediction from (2.16) and corroborate this prediction.

(5A) Computation Results for the Mean Square Dispersion

(5A) 1. *Zero Mean Velocity*

We summarize the computational results for mean square dispersion in the case that $\bar{w}=0$. In this case we will explicitly and accurately account for the sources of error. From (2.9) and (2.14) the mean square dispersion in for $\bar{w}=0$ is simply governed by the velocity structure function which is the incremental variance $R(x, x)$. The total error in estimating $R(x, x)$ via simulation is the sum of the *bias* and the *sampling error*. The bias is the difference between a parameter of the truncated field (e.g., $R^M(x, x)$) and the same parameter of the exact field (e.g., $R(x, x)$). The sampling error is the difference between an estimate of a parameter of the truncated field based on an i.i.d. random sample of a finite size (e.g., $R_r^M(x, x)$) and the true value of the parameter of the truncated field (e.g., $R^M(x, x)$). In the case that $\bar{w}=0$, we will separately consider the bias and the sampling error associated with the velocity structure function.

The number of octaves in the field determines the degree to which the value of the velocity structure function for the truncated field, $R^M(x, x)$ will be biased from the value for the nontruncated field, $R(x, y)$. With the limitations imposed by the truncation formula in (5.1) it was possible to compute the covariance and the velocity structure function of the truncated field without sampling error because the terms

$$\{N(\phi_{mn}^{\sigma\tau}) \mid \sigma = 1, 2, \ldots, \tau \text{ and } m, n \in Z\}$$

are i.i.d. standard normal random variables, so that the terms in the sum are orthogonal. (We do not wish to belabor this point by writing out the lengthy formula, but we do note that the value of $R(x, y)$ for the truncated field is computable by simultaneous binary expansion of x and y, for $x, y \in [0, 1)$.) We will refer to the parameters for the exact (nontruncated) field as *analytic* and those for the truncated field as *semi-analytic*. Thus, the analytic value of the velocity structure function (incremental variance) is $R(x, x)$ and the semi-analytic value of the velocity structure function in an M octave field is $R^M(x, x)$.

We will now investigate the dependence of the bias $(R^M(x, x) - R(x, x))$ on M and x. Figure 1 compares the semi-analytic velocity structure functions to the analytic velocity structure functions, formula (2.13), for 20-, 25-, and 30-octave fields with the dissipation scaling $d = d_0 = 2^{1-M}$.

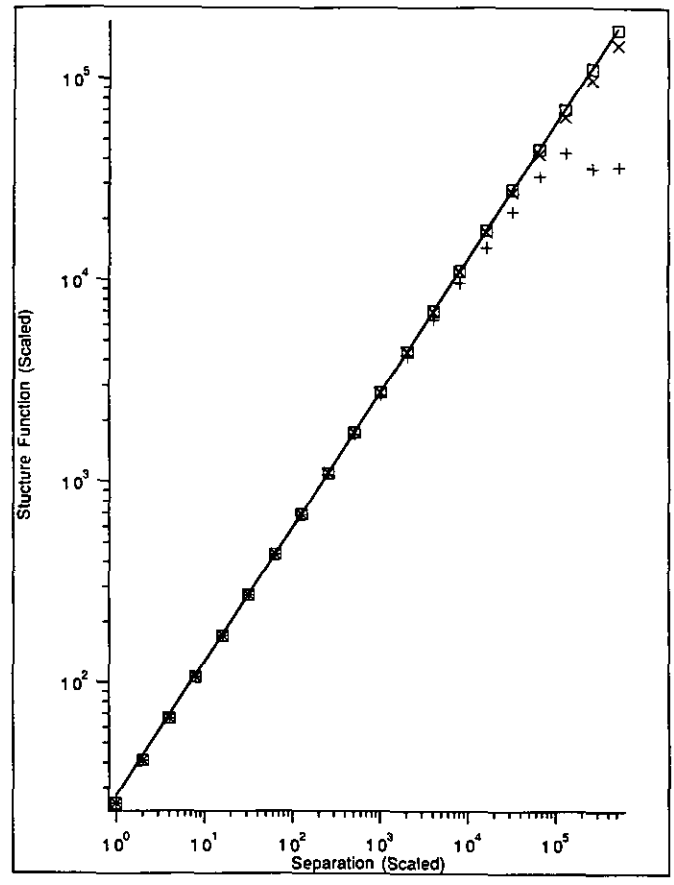

FIG. 1. Velocity structure function vs separation distance without stochastic error for the true field (solid line), a 20-octave field (+), a 25-octave field (×), and a 30-octave field (□); scaling, $d = d_0$.

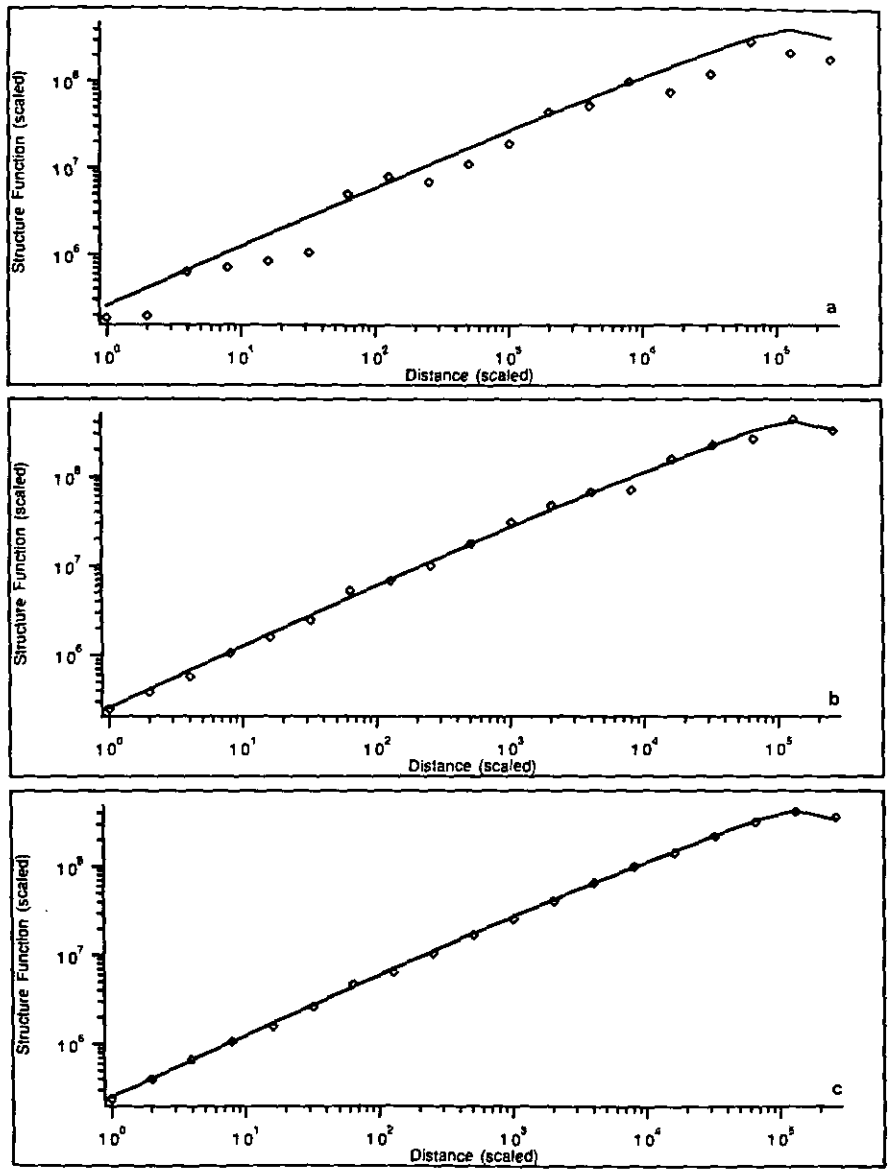

FIG. 2. Velocity structure function vs. separation distance for a 20-octave field without stochastic error (solid line) and with (a) 10, (b) 100, and (c) 1000 realizations ($\diamond$); scaling, $d = d_0$.

Generally, the bias at a particular separation diminishes as the number of octaves of multiwavelets at scales larger than that separation increases; this is not surprising because the energy in the field is greater at larger scales due to infrared divergence. This effect is particularly evident in the large bias in the velocity structure function seen for the 20-octave field at separation distances larger that $2^{13}d$; moreover, this bias is largely absent from the 25- and 30-octave field plots, which have 5 and 10 octaves of multiwavelets at scales larger than $2^{19}d$, the upper limit of the graph. For the 20-octave field the semi-analytic values are within 5% of the analytic values for separations between 2^2d to $2^{10}d$ (2.4 decades), for the 25-octave field the semi-analytic values are within 5% of the analytic values for separations between

TABLE III

Power Law Exponents for the Velocity Structure Function[a]

Number of octaves (M)	Range of fit[b] ($\log_2(x)$)	Number of realizations			
		10	100	1000	∞ (semi-analytic)
20	2-10	0.786	0.693	0.660	0.661
25	2-15	0.606	0.630	0.654	0.664
30	2-19	0.656	0.651	0.660	0.666

[a] Recall that the formula for the velocity structure function is $R(x, x) = \langle (v(x) - v(0))^2 \rangle = K\,|x|^{\varepsilon - 2}$. Because $\varepsilon = \frac{8}{3}$, the analytic value is $\frac{2}{3}$.

[b] The velocity structure function statistics were dissipation scaled. The scaled length x for which the velocity structure function was measured ranged from 2^0 to 2^{M-1}.

2^2d through $2^{15}d$ (3.9 decades), and for the 30-octave field the semi-analytic values are within 5% of the analytic values for separations in octaves 2^2d through $2^{19}d$ (5.1 decades). The 30-octave field has a 1% tolerance region that extends from $x = 2^5d$ to $x = 2^{12}d$ (2.1 decades). As Table III indicates, the power laws derived by least squares fitting of semi-analytic data for the 20-, 25-, and 30-octave fields in the 5% tolerance regions were 0.661, 0.664, and 0.666, respectively, with the analytic value being $\frac{2}{3}$; the power laws associated with fits over the entire range, 2^2d through $2^{19}d$, were 0.554, 0.656, and 0.668 for the 20-, 25-, and 30-octave fields, respectively.

Our multiwavelet expansion allows estimation of the velocity structure function (incremental variance) with very small stochastic error $(R_r^M(x, x) - R^M(x, x))$ as indicated by Table III and Fig. 2 through 4. These figures describe Monte Carlo simulations of mean square dispersion statistics for 20, 25, and 30 octaves with 10, 100, 1000 realizations, as noted. For the sample size 100, the estimated values are fairly close to the semi-analytic values so that, as Table III indicates, the power law fits over the 5% bias tolerance ranges are 0.693, 0.630, and 0.651 for the 20-, 25-, and 30-octave fields, respectively. For the sample size 1000 the estimated values are almost indistinguishable from the semi-analytic values so that the power law fits over the 5% bias tolerance ranges are 0.660, 0.654, and 0.660 for the 20-,

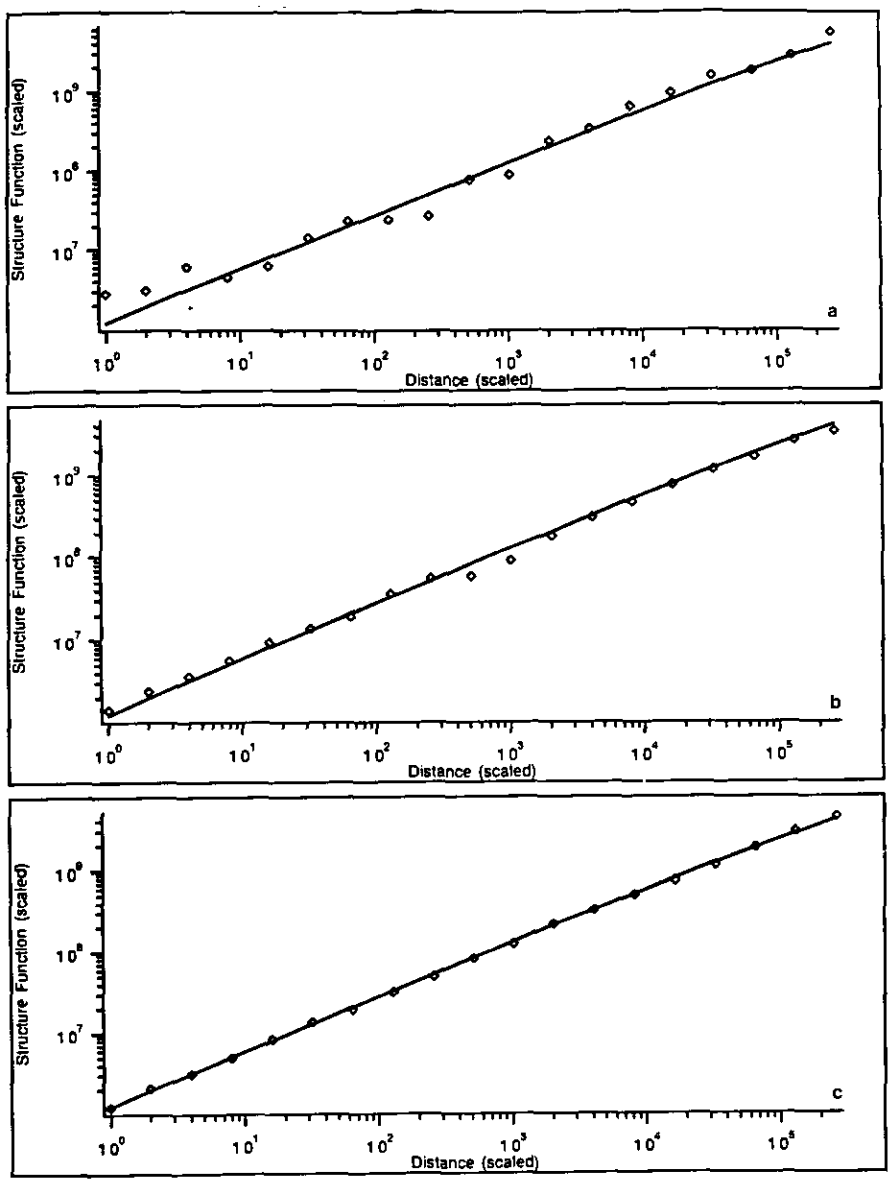

FIG. 3. Velocity structure function vs separation distance for a 25-octave field (see Fig. 2).

25-, and 30-octave fields, respectively. None of these power laws has more than a 2% error with respect to the analytic power law.

The small sampling errors for the velocity structure function (incremental variance) can be quantified rigorously. Because $v(x)-v(0)$ and its truncated approximation $v^M(x)-v^M(0)$ are Gaussian with mean 0, the estimator for the velocity structure function has a gamma distribution. Therefore, with $R_r^M(x,x)=(1/r)\sum_{i=1}^{r}(v_i^M(x)-v_i^M(0))^2$ the quantity

$$Z=\frac{R_r^M(x,x)}{R^M(x,x)}$$

has the cumulative distribution function

$$P(Z\leqslant z)=\int_0^z \frac{y^{\alpha-1}e^{-y/\beta}}{\beta^\alpha\Gamma(\alpha)}\,dy$$

with $\alpha=r/2$ and $\beta=2/r$. Table IV gives the probability of exceeding certain percentages of error for several sample sizes according to this distribution. This indicates that high accuracy is possible for moderate sample sizes; for example, an error of 10% or less has a probability of 0.975 for a sample size of 1000 and an error of 5% or less has a probability of 0.975 for a sample size of 4000.

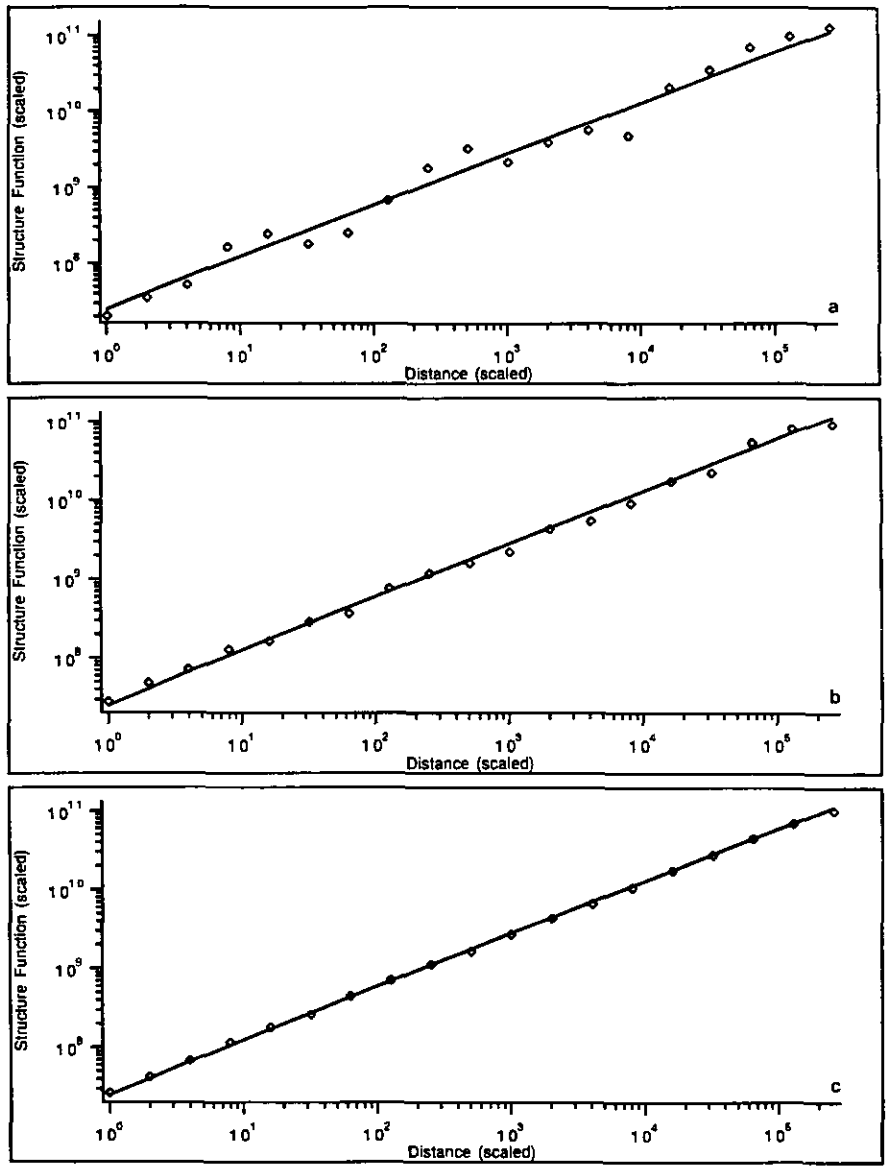

FIG. 4. Velocity structure function vs separation distance for a 30-octave field (see Fig. 2).

As one would expect from the previous observations, the simulations of mean square dispersion for $\bar{w} = 0$ are generally very accurate. Figures 5a through 5d give the results of the simulation of mean square dispersion with initial separations x of $10d$ through $10^4 d$ with $d = 16d_0$ and $M = 30$. As indicated, the graphs compare the analytic predictions with the results from 1000 realizations. As one would expect from formula (2.9) the errors are constant with respect to time because they are dependent only on the estimate of $R(x, x)$, which determines the amplitude of these parabolas. The results are generally quite satisfactory with errors on the order of 1%; however, an atypical sampling error of 9% was observed for one simulation of mean square dispersion for $\bar{w} = 0$.

Since the particles started at $(0, 0)$ and $(x, 0)$ have constant velocities in each realization, the step size for the integration is irrelevant for $\bar{w} = 0$. Nevertheless, step size was an important consideration for the estimation of mean square dispersion when $\bar{w} \neq 0$.

(5A) 2. *Non-zero Mean Velocity*

We will now consider mean square dispersion in the case that $\bar{w} \neq 0$. By symmetry we assume that $\bar{w} > 0$ and without

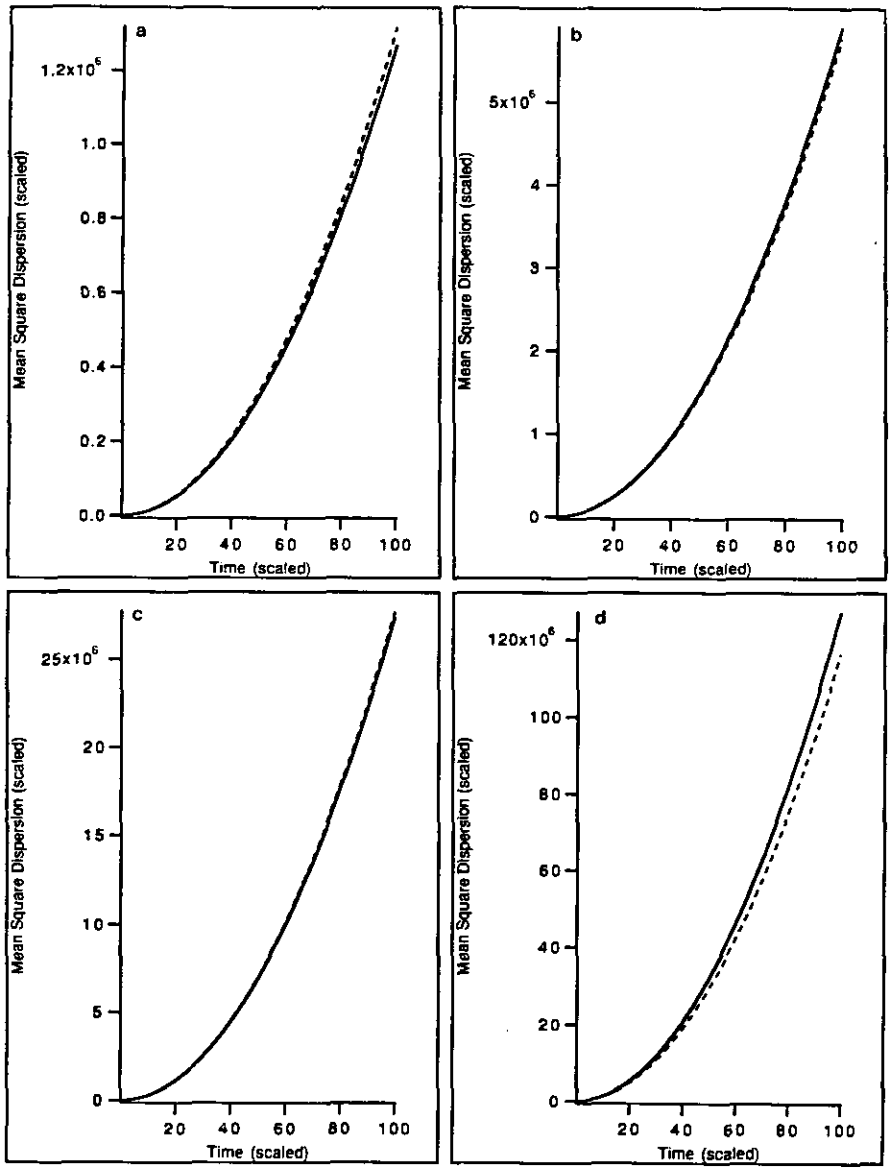

FIG. 5. Mean square dispersion vs time with $\bar{w} = 0$ and initial separation x equal to (a) $10d$, (b) $10^2 d$, (c) $10^3 d$, and (d) $10^4 d$; realizations, 1000; integration step size, $h = 0.2d$; scaling, $d = 16d_0$.

TABLE IV

Probability of Exceeding a Given Error in Estimating the Velocity Structure Function

Error level (percentage)	Number of realizations	Probability of excess error[a]
25	100	7.51716×10^{-2}
25	250	5.57894×10^{-3}
25	500	1.22128×10^{-4}
25	1000	$< 10^{-6}$
10	100	4.79007×10^{-1}
10	250	2.62740×10^{-1}
10	500	1.13364×10^{-1}
10	1000	2.53316×10^{-2}
10	2000	1.60923×10^{-3}
10	4000	9.06070×10^{-6}
10	8000	$< 10^{-6}$
5	100	7.23917×10^{-1}
5	250	5.76129×10^{-1}
5	500	4.29036×10^{-1}
5	1000	2.63350×10^{-1}
5	2000	1.13726×10^{-1}
5	4000	2.53433×10^{-2}
5	8000	1.57638×10^{-3}

[a] Probabilities less than 10^{-6} could not be calculated accurately because of numerical instability. The range of values listed was verified through comparison with high precision calculations done in *Mathematica*.

loss of generality we set $\bar{w} = 1$. When $\bar{w} = 1$, the y-position of a particle is determined by the integral of $v(\cdot)$,

$$Y(t) = y_0 + \int_0^t v(s + x_0)\, ds.$$

In our simulations we integrated $v(\cdot)$ using the trapezoidal rule to determine the relative y displacement of the two test particles.

The results for mean square dispersion with $\bar{w} = 1$ were generally accurate, especially for initial separations, x, much greater than the dissipation scale, d_0. Figures 6 through 9 give the results of the simulation of mean square dispersion with $\bar{w} = 1$ and initial separations x of $10d$ through $10^4 d$, a maximum time of 100, an integration step size of $0.2d$, a scale $d = 16d_0$, and number of octaves $M = 30$. The "a" graphs compare the values estimated with 1000 realizations to the analytic values given by formula (2.10); the "b" graphs show the ratio of the estimated values to the analytic values. Figure 6b with a separation of $10d$ indicates a maximum absolute error of 6% with much oscillation in this error. This effect diminishes as the initial separation becomes much larger than the dissipation scale d_0. Figure 7b with a separation of $100d$ shows a maximum absolute error of 3%, and Figs. 8b and 9b with separations of $1000d$ and $10000d$, respectively, show maximum absolute errors of 1%.

To demonstrate that the errors encountered in Figs. 6 through 9 were not due to the integration step size, we repeated the simulations with a step size one-tenth as large and for a time one-tenth as long. Accordingly, Figs. 10 through 13 give the results of the simulation of mean square dispersion with $\bar{w} = 1$ and initial separations x of $10d$ through $10^4 d$, a maximum time of 10, an integration step size of $0.02d$, a scale $d = 16d_0$, and number of octaves $M = 30$. Again, the "a" graphs compare the values estimated with 1000 realizations to the analytic values given by formula (2.10): the "b" graphs show the ratio or the estimated values to the analytic values. Refining the integration step size did not change the error history in the first 10 time units in any study.

(5A) 3. *The Choice of Integration Step Size*

For the computation of mean square dispersion with a nonzero mean flow, choosing the largest integration time

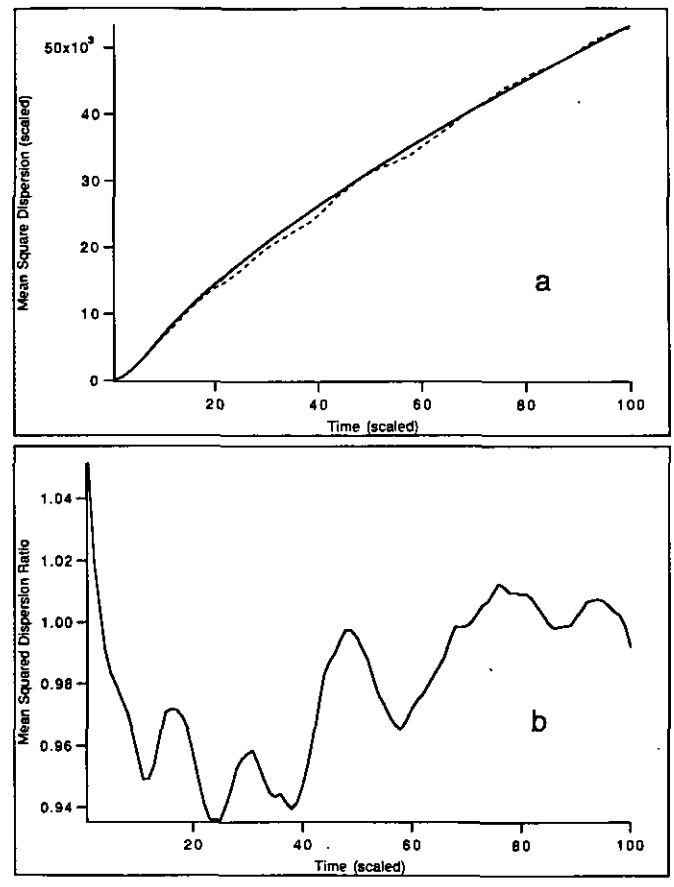

FIG. 6. Mean square dispersion study with $\bar{w} = 1$. Parameters $x = 10d$, $h = 0.2d$, and $d = 16d_0$: (a) Mean square dispersion vs time. (Solid line indicates analytic value. Dotted line indicates value from 1000 realizations.) (b) The ratio of simulated to analytic mean square dispersion vs time. (Note that the absolute error is never more than 6.0%.)

step for a given level of error is necessary to minimize the running time of the simulation. In order to determine an adequate step size, we will account for each error in the calculation separately. For $\bar{w} = 1$ mean square dispersion is approximated by the formula

$$\langle l_y^2 \rangle(t, x) \simeq \left\langle \left(\sum_{j=0}^{n} v(jh + x)\, m_j - v(jh)\, m_j \right)^2 \right\rangle \quad (5.2a)$$

for $h = t/n$ and

$$m_j = \begin{cases} h/2, & \text{if } j = 0, n; \\ h, & \text{otherwise.} \end{cases} \quad (5.2b)$$

The resulting quadrature formula (5.2a) can be written in terms of incremental covariance, $R(\cdot, \cdot)$ (given by formula (2.12)), which can then be approximated by incremental covariance of the truncated field, $R^M(\cdot, \cdot)$, as in formula (5.3b) below. The incremental covariance of the truncated field can then be approximated by an r-sample estimate, $R_r^M(\cdot, \cdot)$, as in formula (5.3c) below. All of this is summarized in the sequence of approximations,

$$\langle l_y^2 \rangle(t, x) \simeq \sum_{j,k=0}^{n} (R(jh, kh) + R(jh + x, kh + x) - 2R(jh, kh + x))\, m_j m_k \quad (5.3a)$$

$$\simeq \sum_{j,k=0}^{n} (R^M(jh, kh) + R^M(jh + x, kh + x) - 2R^M(jh, kh + x))\, m_j m_k \quad (5.3b)$$

$$\simeq \sum_{j,k=0}^{n} (R_r^M(jh, kh) + R_r^M(jh + x, kh + x) - 2R_r^M(jh, kh + x))\, m_j m_k, \quad (5.3c)$$

where $\simeq$ denotes approximate equality. These formulas, (5.3a), (5.3b), and (5.3c), are exactly computable, and we calculated their values numerically to determine several different kinds of error to better analyze and control the total error. The *integration error* is the error in approximating

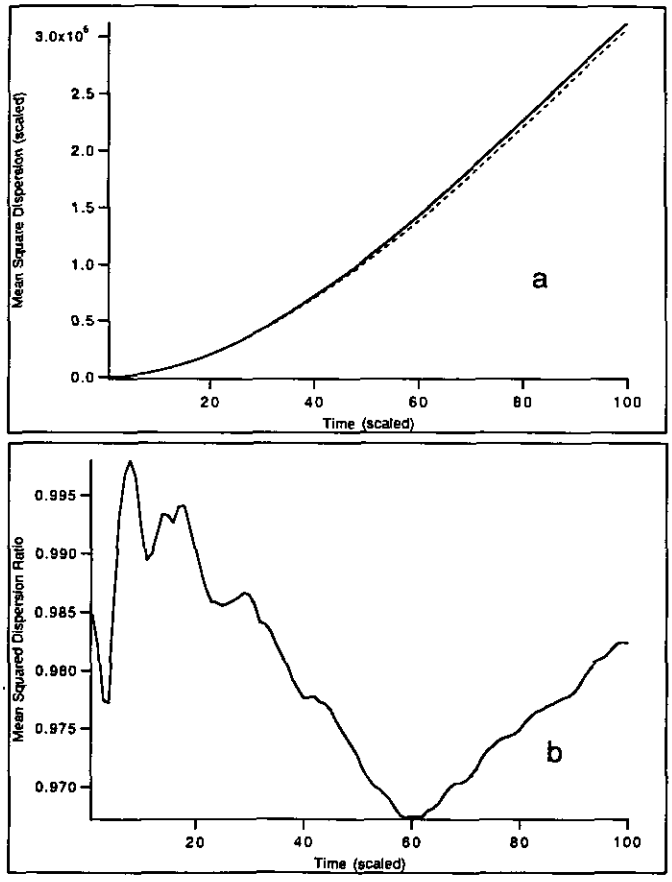

FIG. 7. Same as Fig. 6 except that $x = 10^2 d$. (Note that the absolute error is never more than 3.5%.)

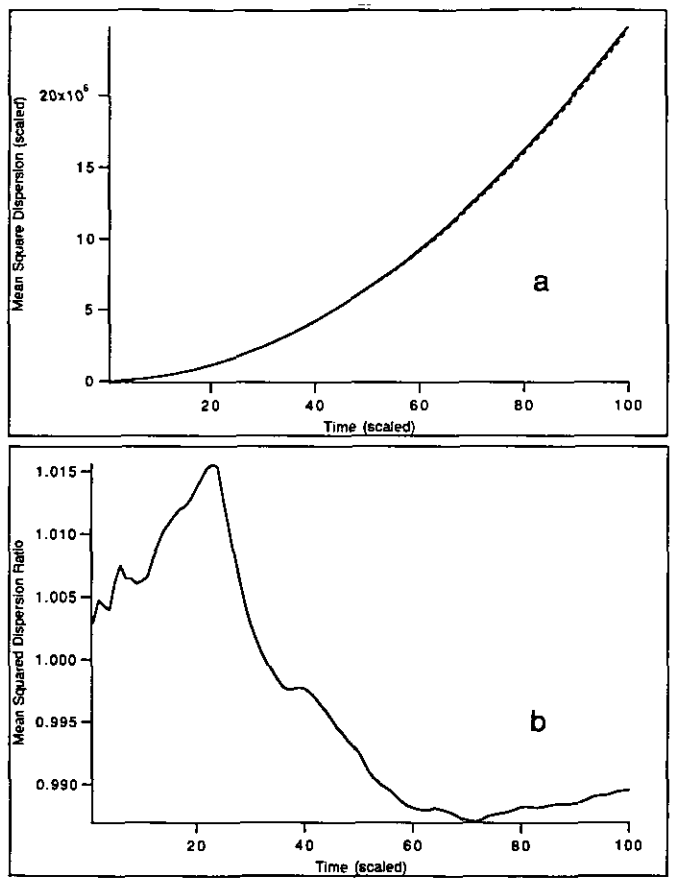

FIG. 8. Same as Fig. 6 except that $x = 10^3 d$. (Note that the absolute error is never more than 1.5%.)

mean square dispersion by formula (5.3a), the *truncation error* is the error in approximating formula (5.3a) by formula (5.3b), the *sampling error* is the error in approximating (5.3b) by (5.3c), and the *total error* in simulation is the error in approximating mean square dispersion by (5.3c). We present these errors as relative errors (i.e., divided by the true value from formula (2.10)).

Just as the mean square dispersion formula in (2.10) is homogeneous of degree ε in x and t, the quadrature approximation, formula (5.3a) is homogeneous of degree ε; this determines a time step size criterion for computing mean square dispersion. If we multiply x and t by λ, then m_i and m_j scale like λ and each incremental covariance term scales like $\lambda^{\varepsilon-2}$ and, therefore, the overall approximation (5.3a) of the mean square dispersion scales like λ^{ε}. Accordingly, the percent error in formula (5.3a), the integration error, depends only on the ratio of h to x.

We investigate the dependence of the relative error on h and x for a 30-octave field through Monte Carlo simulations with 1000 realizations. All figures that we present are on the scale $d = 16d_0$ for $d_0 = 2^{-29}$. In all figures part "a" represents a comparison of the stochastic estimate to the analytic formula (2.10) and part "b" represents the total error in the stochastic estimate with respect to the analytic formula to provide an error history. Where necessary, we also indicate the dominant component (sampling, truncation, or integration) of the total error as a dotted line on the graph. The same 1000 realizations were used in all cases for the sake of comparison.

We computed mean square dispersion for separations x of $10d$, 10^2d, 10^3d, and 10^4d, time step sizes h of $0.2x$, $0.1x$, and $0.05x$, and maximum times t of $1.6x$. (A longer time could not be simulated on the largest scale because of restrictions on the number of random numbers available in our workstation calculations.) We found that $h = 0.2x$ was a sufficiently small step size to ensure that the integration error was smaller than the sampling error for 1000 realizations. Figure 14 ($x = 100d$ and $h = 20d$) shows a total error which is never more than 5.5% in absolute value and usually less than 3%. Figure 15 ($x = 1000d$ and $h = 200d$) shows a total error which is never more than 4.0% in absolute value and usually less than 1% in absolute value.

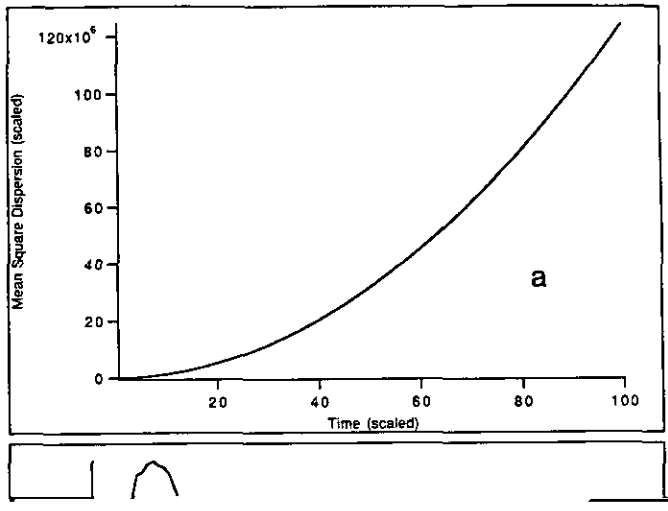

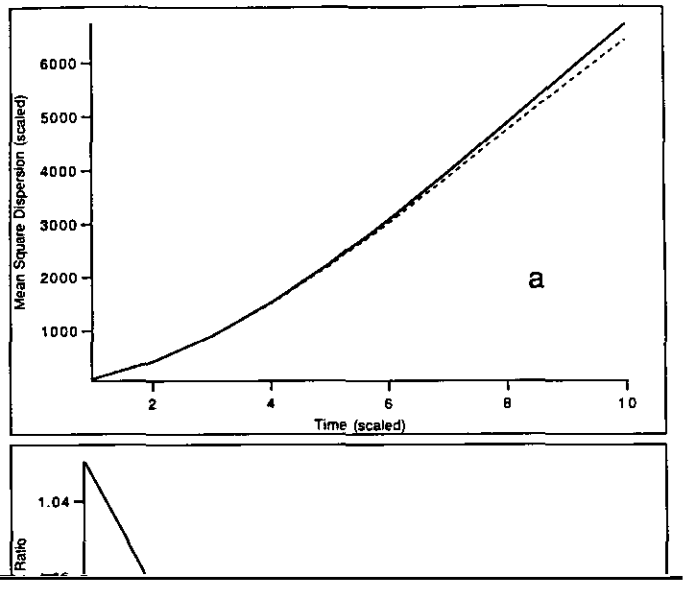

Figure 16 ($x = 10000d$ and $h = 2000d$) shows a total error which is never more than 8.5% in absolute value and usually less than 4% in absolute value. In all three cases, the worst total error is at the beginning of the run because for the first time step the integration error is roughly 3% but decreases rapidly thereafter. In Fig. 16 more than 5% of the total error (solid line) at the beginning of the run is due to sampling error (dotted line). For this collection of $r = 1000$ samples, $R_r^M(0, 10^4 d)$ is roughly 8% less than the expected value; this is a sampling artifact. Such artifacts, while not common, can occur at various locations in the sample of fields for various random seeds for the program.

As a practical time step criterion, we find that a time step size of $h = 0.2x$ is necessary (up to a factor of 2) and sufficient to ensure that, for all separation distances, the integration error does not significantly contribute to the total error. Figure 17 ($x = 1000d$ and $h = 100d = 0.1x$) and Fig. 18 ($x = 1000d$ and $h = 50d = 0.05x$), with relative errors of order 1.5% and 2.5%, show error histories similar to that of Fig. 15 ($x = 1000d$ and $h = 200d$), indicating that the integral is close to convergence for $h = 200d$. Figures 19 and 20 also show the dominant components of their total errors (sampling, truncation, or integration errors computed from formula (5.3)) as additional plots in part "b". Figure 19 indicates that for a separation of $x = 1000d$, $h = 400d = 0.4x$ is too large. The total error (solid line), which is dominated by integration error (dotted line), increased steadily to more than 15% at time $8000d$. However, with an integration step size of $h = 200d = 0.2x$ and the same separation, Fig. 20 indicates that the total error (solid line) is never more than 8% for a maximum time of $16000d$. Moreover, the error in this run was dominated by the sampling error (dotted line).

Formulas (5.3a), (5.3b), and (5.3c) make a rigorous and detailed error analysis possible; this analysis suggests criteria for selecting the time step size. Table V ($x = 1000d$ and $h = 400d = 0.4x$) and Table VI ($x = 1000d$ and $h = 200d = 0.2x$) are analyses of the percent of sampling, truncation, and integration error composing the total error in the first $3200d$ time units of the runs depicted in Figs. 19 and 20, respectively. Again, the dominant error for the step size $h = 0.4x$ is an integration error which increases steadily from -4.4% to 12.4%, while the sampling error is no more than 6% in absolute value. The dominant error for the step size $h = 0.2x$ is sampling error, while the integration error

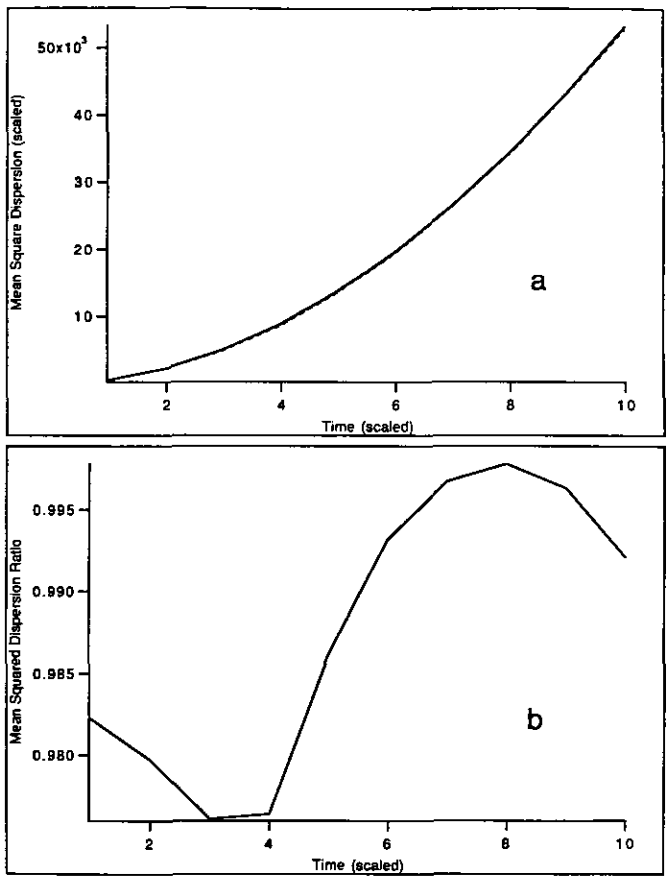

FIG. 11. Same as Fig. 10 except that $x = 10^2 d$. Compare Figs. 11b and 7b.

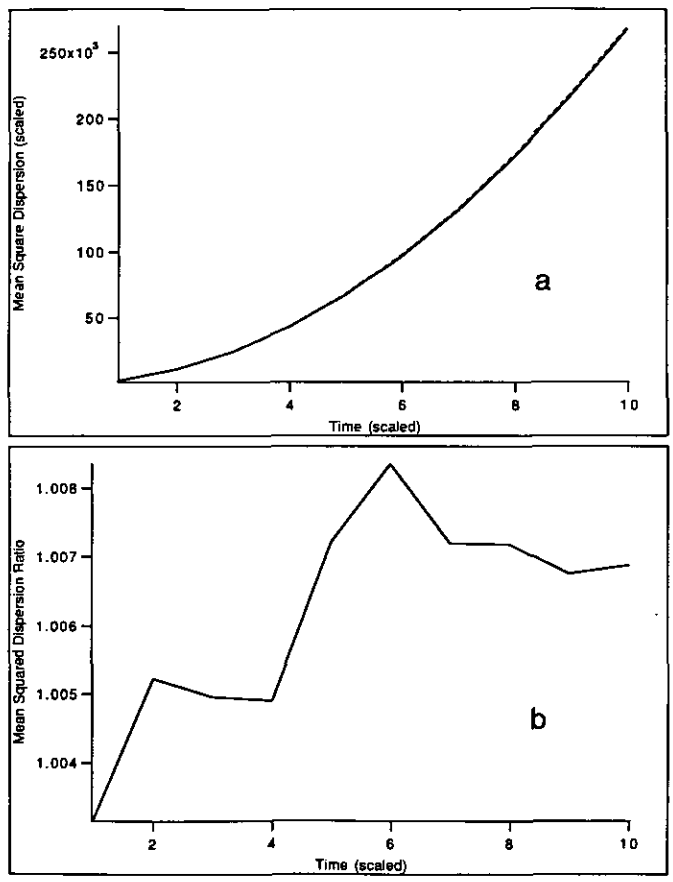

FIG. 12. Same as Fig. 10 except that $x = 10^3 d$. Compare Figs. 12b and 8b.

decreases in absolute value for every time step after $800d$. This suggests that the time step be chosen small enough so that the integration error does not increase with time and so that the integration error is smaller than the sampling error and leads to the practical criterion, $h = 0.2x$, which we utilized above. Since the truncation error is less than 0.515% in absolute value, so that it contributes negligibly to the total error, choosing the integration step size according to the above criteria will ensure nearly optimal results.

(5B) Computations for Mean Square Displacement

Here we consider the mean square displacement of a particle advected by a velocity field $v_M(\cdot)$ with the scale truncation

$$v_M(x) = \sum_{\sigma=1}^{\tau} \sum_{m=0}^{M-1} \sum_{|n - \lfloor 2^m x \rfloor| r_m} 2^{m(-1/2-\lambda)} \times (G * \phi^{\sigma\tau})(2^m x - n)\, N(\phi_{mn}^{\sigma\tau}). \tag{5.4}$$

(Such a field contains the unit scale and $M-1$ larger scales; there is a slight change in notation which should not confuse the reader.) This choice of scaling mimics the behavior of the cutoff field from (2.3) which is essential to recover the theoretical limiting behavior of the mean square displacement from (2.16). We will assume a non-zero mean velocity $\bar{w}$, and, without loss of generality, we will also assume that $\bar{w} = 1$. Under these conditions, the displacement in the y-direction is

$$Y_M(t) = \int_0^t v_M(s)\, ds \tag{5.5}$$

and the mean square displacement is

$$\langle Y_M(t)^2 \rangle = \left\langle \int_0^t \int_0^t v_M(r)\, v_M(s)\, dr\, ds \right\rangle = \int_0^t \int_0^t \langle v_M(r)\, v_M(s) \rangle\, dr\, ds = \int_0^t \int_0^t \tilde{R}_M(r, s)\, dr\, ds, \tag{5.6}$$

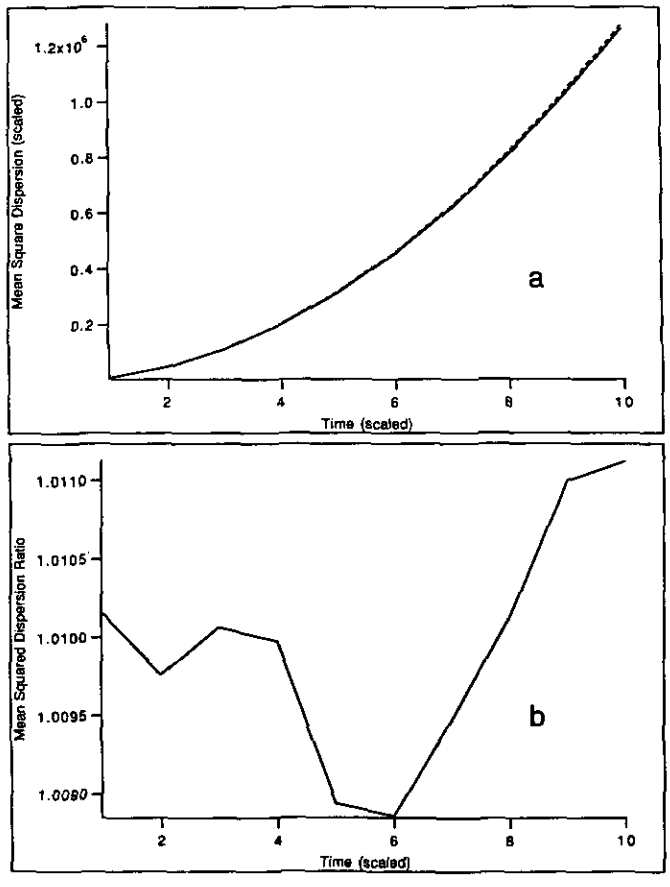

FIG. 13. Same as Fig. 10 except that $x = 10^4 d$. Compare Figs. 13b and 9b.

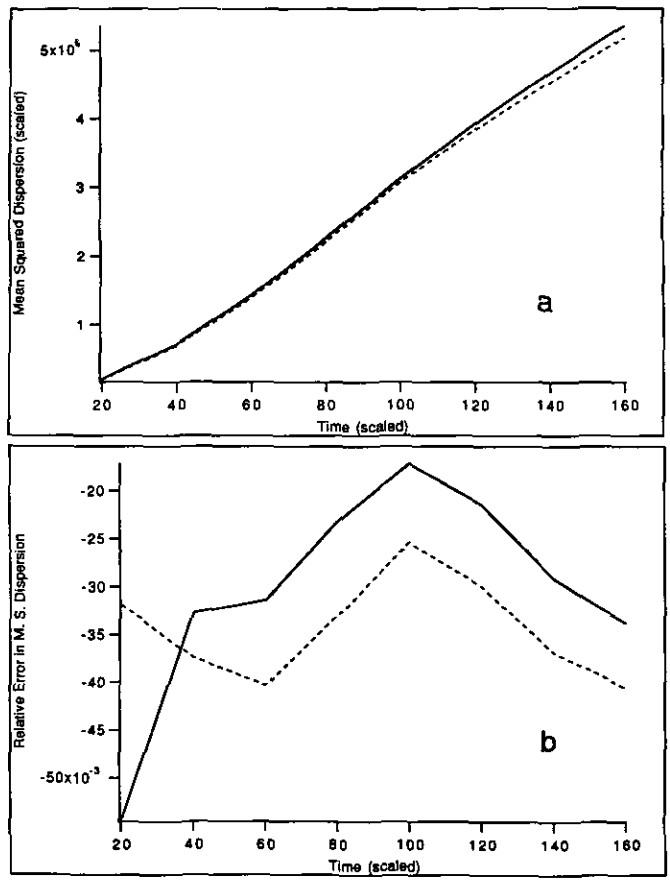

FIG. 14. Mean square dispersion study with $\bar{w} = 1$. Parameters $x = 10^2 d$, $h = 0.2x$, and $d = 16 d_0$. (a) Mean square dispersion vs time. (Solid line indicates analytic value. Dotted line indicates value from 1000 realizations.) (b) Relative error in mean square dispersion vs time. (Solid line indicates total error; dotted line indicates sampling error (dominant). Note that the absolute error is never more than 5.5%.)

where

$$\tilde{R}_M(r, s) = \langle v_M(r)\, v_M(s) \rangle \tag{5.7}$$

is the covariance of $v_M(\cdot)$. Of course, the mean square displacement of a particle transported by a nontruncated velocity field would not be defined because the covariance function $\tilde{R}(r, s)$ would not be defined due to the strong infrared divergence of the spectrum. Instead we have the rigorous theoretical prediction from (2.16) for the mean square displacement as $\delta \to 0$. Thus, in accordance with this prediction, the mean square displacements, $\langle Y_M(t)^2 \rangle$, should satisfy

$$\left| \frac{\langle Y_M(t)^2 \rangle}{\tilde{R}_M(0, 0)\, t^2} - 1 \right| \leqslant \theta, \tag{5.8}$$

for any θ, $T > 0$, $0 \leqslant t \leqslant T$, and all M sufficiently large.

By using truncated fields of the form $v_M(\cdot)$ given by Eq. (5.4) and normalizing them according to formula (5.8) we can determine the time interval $[0, T]$ for which formula (5.8) gives a good estimate of the mean square displacement. Since the covariance

$$\tilde{R}_M(r, s) = \langle v_M(r)\, v_M(s) \rangle \tag{5.9}$$

is computable from formula (5.4), we are able to compute mean square displacement for $v_M(\cdot)$, $\langle Y_M(t)^2 \rangle$ through trapezoidal integration without stochastic error. Because displacement statistics are only defined for truncated fields, we denote the exact displacement statistics computed for truncated fields as "analytic."

We will now compare the analytic data for fields with varying numbers of octaves to the theoretical prediction of formula (5.8). Figure 21 shows the result of mean square displacement with a dissipation scaling (for the sake of comparison) followed by normalization according to formula (5.8) for $M = 15, 20, 25, 30$; in each case the integration step size is 64 times the dissipation scale d_0 and the number of time steps is 100. For the 15-octave field, the scaled mean square displacement decreased rapidly. The scaled mean square displacement was down to 0.82 by time

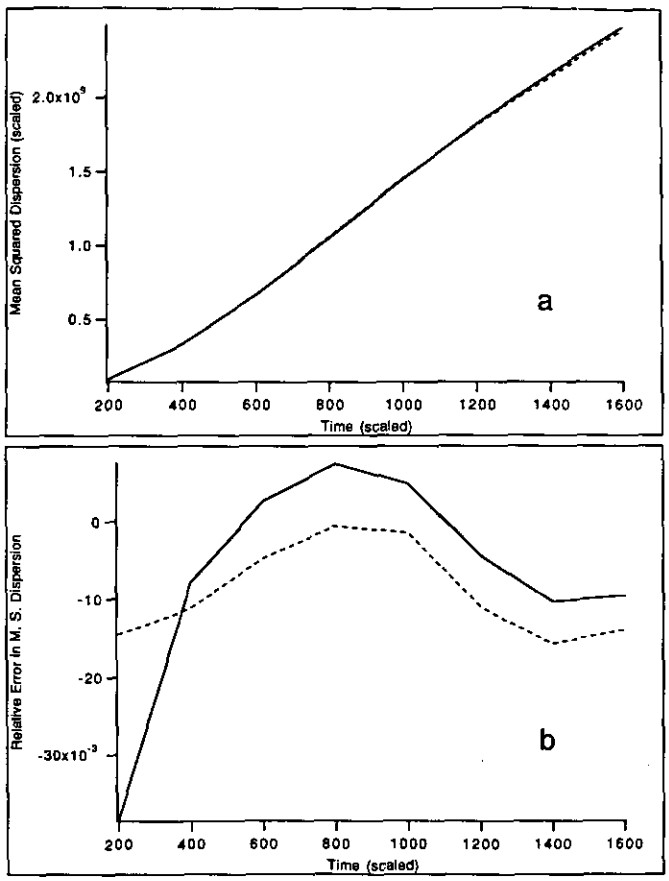

FIG. 15. Same as Fig. 14 except that $x = 10^3 d$. (Note that the absolute error is never more than 4% and usually less than 1%.)

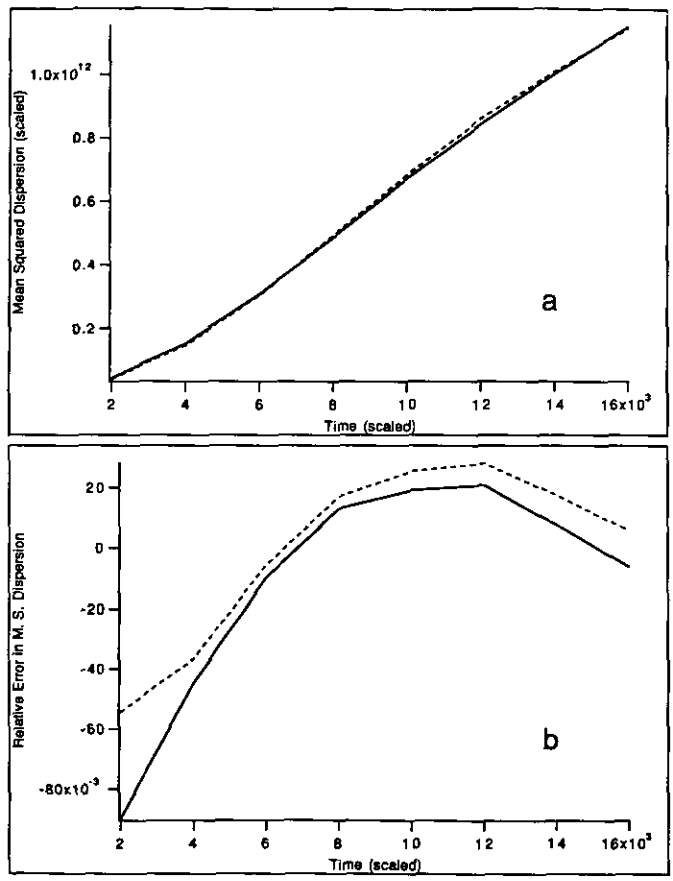

FIG. 16. Same as Fig. 14 except that $x = 10^4 d$. (Note that the absolute error is never more than 8.5% and usually less than 4%.)

$t = 64d_0$; by time $t = 1500d_0$ the scaled mean square displacement is less than 0.20, and thereafter, the measured value did not exceed 0.20. For the 20-octave field, the scaled mean square displacement decreased steadily to approximately 0.69 at $t = 6400d_0$. For the 25-octave field, the scaled mean square displacement remained between 0.97 and 1.00 throughout the run. For the 30-octave field the scaled mean square displacement remained between 0.995 and 1.000. These results obviously corroborate the theoretical prediction in (5.8) and converge as M increases.

These graphs give quantitative information about the useful range of formula (5.8) for various truncations and maximum times. For $T = 6400d_0$, formula (5.8) applies with $\theta \leqslant 0.10$ only when $M \geqslant 25$. For $T = 640d_0$, formula (5.8) applies with $\theta \leqslant 0.10$ only when $M \geqslant 20$. For $T = 64d_0$, formula (5.8) applies with $\theta \leqslant 0.10$ when $M \geqslant 15$.

All of the data in Figure 21 were computed without stochastic error; Figs. 22a through 22d compare scaled mean square displacement computed by simulation with 1000 realizations to the analytic data discussed above. For the 15- and 20-octave fields, Figs. 22a and 22b show an oscillation of the simulated scaled mean square displacement about the analytic value; 80% of the data points are within $\pm 7\%$ of the analytic value. For the 25-octave field, Fig. 22c shows that the simulated value is consistently above the analytic value, but by no more than 4%. For the 30-octave field, Fig. 22d shows that the simulated value is consistently below the analytic value, but by no more than 4%. This contrast in the pattern of error between the first two figures and the second two figures of this series shows that the presence of large scale wavelets in the field representation causes stochastic error to persist at a particular value.

6. CONCLUDING REMARKS

We have designed a new Monte Carlo method for the difficult problems of turbulent diffusion involving random velocity fields, long range correlations, and infrared divergence. This method is based on judicious use of scaling and localization through a compact explicit truncated expansion involving Alpert–Rokhlin multiwavelets with

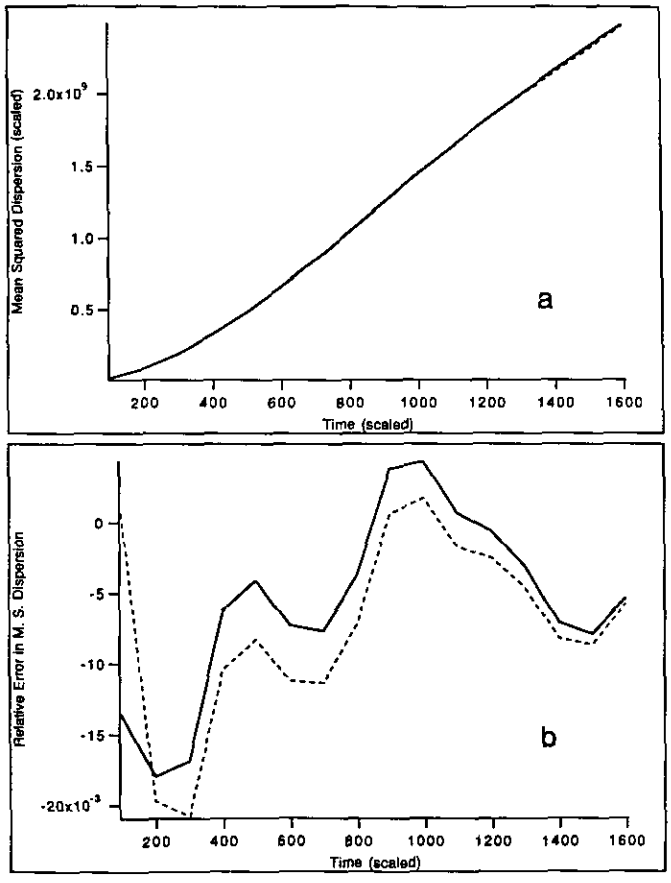

FIG. 17. Mean square dispersion study with $\bar{w} = 1$. Parameters $x = 10^3 d$, $h = 0.1x = 10^2 d$, and $d = 16d_0$. (a) Mean square dispersion vs time. (Solid line indicates analytic value. Dotted line indicates value from 1000 realizations.) (b) Relative error in mean square dispersion vs time. (Solid line indicates total error; dotted line indicates sampling error (dominant).) Compare Figs. 17b and 15b.

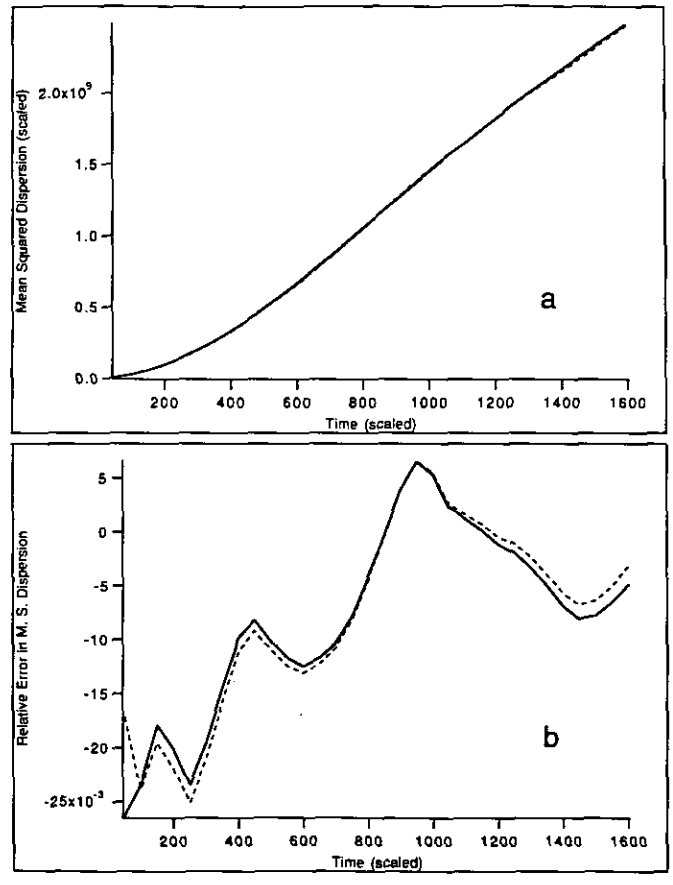

FIG. 18. Same as Fig. 17 except that $x = 50d$. Compare Figs. 18b and 15b.

high moment cancellation (Section 3), together with a recursive scheme of random number generation with minimal storage which exploits the special structure of the truncated expansion (Section 4). The principle for a priori truncation of this expansion is a sharp, mathematically rigorous statistical energy criterion (Section 3) which has been applied in Sections 3 and 5.

The new wavelet Monte Carlo method was validated on an exactly solvable but nontrivial test problem (Section 2, [10, 11]) with infrared divergences and long range velocity correlations. The computational results for such sensitive quantities as the velocity structure function and the scalar mean square dispersion in the model problem are very encouraging. Not only the scaling exponents but even the numerical values of these quantities were simulated within a few percent over five decades of separation distance with modest numbers of elements (792) and small numbers of realizations (100 to 1000) on a local workstation. Furthermore, these computational results were presented within a theoretical statistical framework which elucidated the sources of various analytic, sampling, and time stepping errors.

With the low variance and compact accurate representation of the random field developed here in a simple model problem, an important future direction is the development of this method for multidimensional incompressible random velocity fields. Such extensions have recently been developed by the authors [12, 13] and will be reported in a series of publications in the near future.

APPENDIX A: INTEGRALS OF SQUARE INTEGRABLE FUNCTIONS WITH RESPECT TO BROWNIAN MOTION

Because the velocity field v was defined in terms of an integral with respect to Brownian motion, we review the essential properties of integrals of functions with respect to Brownian motion. Since we require these integrals to have finite variance, we use only square integrable functions as integrators. We require none of the path properties of Brownian motion; therefore, we do not define it but refer the reader to any good text in elementary random process theory. Rather, we consider an integral with respect to

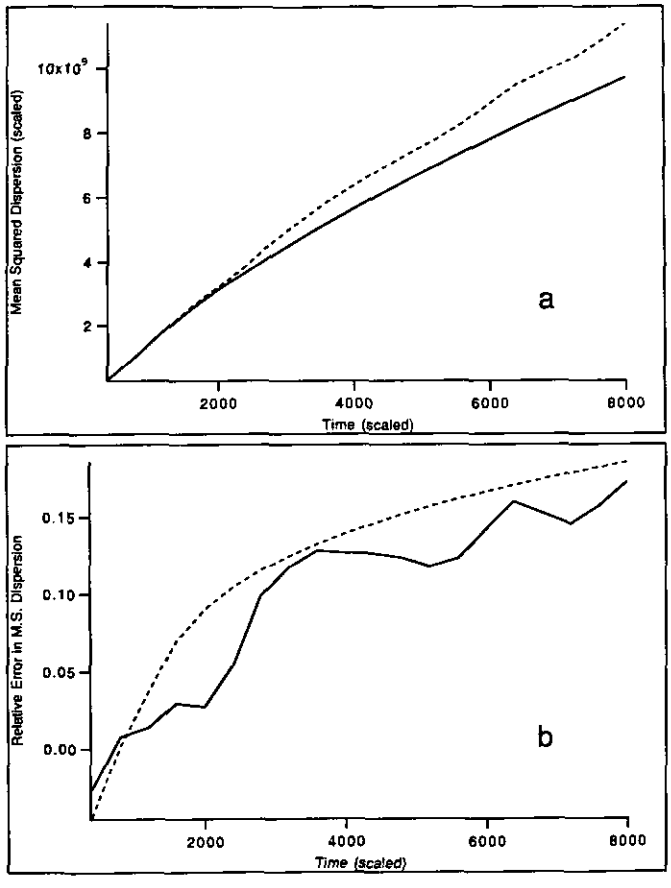

FIG. 19. Mean square dispersion study with $\bar{w} = 1$. Parameters $x = 10^3 d$, $h = 0.4x = 4 \times 10^2 d$, and $d = 16 d_0$. In (b) the dotted line indicates integration error, which is dominant.

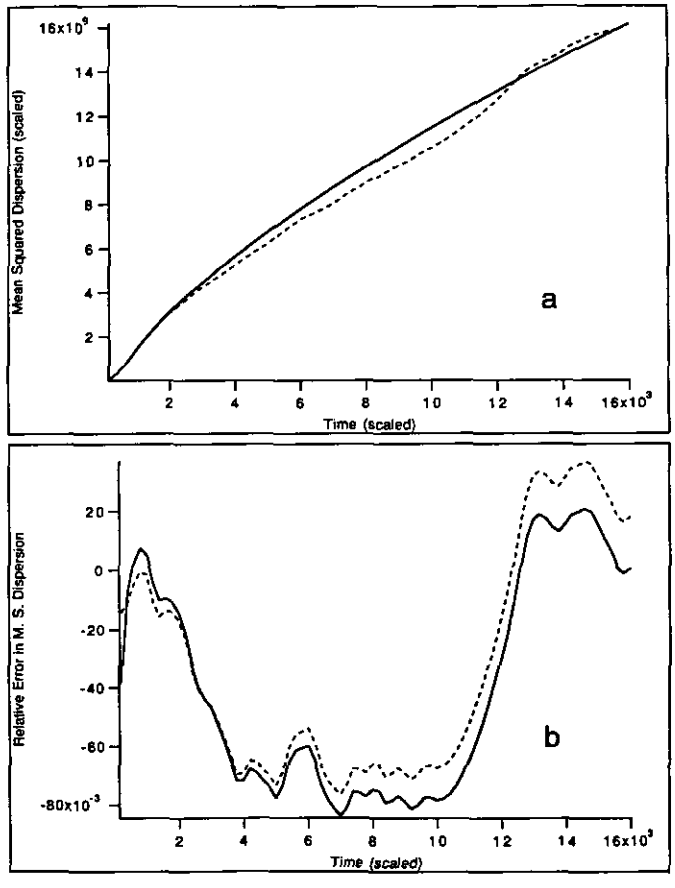

FIG. 20. Means square dispersion study with $\bar{w} = 1$. Parameters $x = 10^3 d$, $h = 0.2x = 2 \times 10^2 d$, and $d = 16 d_0$. In (b) the dotted line indicates sampling error, which is dominant.

TABLE V

Error Analysis for Mean Square Dispersion with Initial Separation $1000d$ and Time Step $400d$

Time (scaled)	Error			
	Sampling (percentage)	Truncation (percentage)	Integration (percentage)	Total (percentage)
400	2.018	−0.203	−4.440	−2.625
800	0.828	−0.219	0.170	0.779
1200	−1.983	−0.256	3.612	1.374
1600	−3.733	−0.306	6.989	2.951
2000	−5.885	−0.358	8.977	2.734
2400	−4.641	−0.411	10.396	5.344
2800	−1.188	−0.463	11.508	9.857
3200	−0.222	−0.515	12.430	11.693

Brownian motion to be a linear map which maps a square integrable function to a Gaussian random variable; we refer to this map as *white noise* (Ref. [27]).

We begin by reviewing some terminology about square integrable functions. A real or complex function f on the real line R is said to be *square integrable* if it has *norm*

$$\|f\| = \left(\int_{-\infty}^{\infty} |f(x)|^2 \, dx \right)^{1/2} \tag{A.1}$$

less than infinity; the *inner product* of two square integrable functions is defined by

$$(f, g) = \int_{-\infty}^{\infty} f(x) \, \overline{g(x)} \, dx. \tag{A.2}$$

TABLE VI

Error Analysis for Mean Square Dispersion with Initial Separation $1000d$ and Time Step $200d$

Time (scaled)	Error			
	Sampling (percentage)	Truncation (percentage)	Integration (percentage)	Total (percentage)
200	5.023	−0.193	−2.200	−2.630
400	2.922	−0.194	0.516	3.244
600	0.451	−0.201	0.936	1.187
800	−1.279	−0.212	1.019	−0.472
1000	−1.146	−0.228	0.862	−0.511
1200	−0.890	−0.249	0.905	−0.234
1400	−2.114	−0.273	0.810	−1.577
1600	−3.086	−0.299	0.729	−2.656
1800	−3.685	−0.324	0.663	−3.346
2000	−4.804	−0.350	0.608	−4.546
2200	−4.923	−0.376	0.564	−4.736
2400	−3.317	−0.402	0.525	−3.194
2600	−1.089	−0.428	0.493	−1.024
2800	0.495	0.454	0.465	0.505
3000	1.619	−0.480	0.440	1.579
3200	2.381	−0.506	0.418	2.294

The collection of square integrable functions is a linear space, $L^2(R)$. An *orthonormal basis* for $L^2(R)$ is a countable collection of square integrable functions $\{\phi_n \mid n = 0, 1, 2, \ldots\}$ which satisfies

$$(\phi_m, \phi_n) = \begin{cases} 1, & \text{if } m = n; \\ 0, & \text{otherwise.} \end{cases}$$
$$= \delta_{mn} \tag{A.3}$$
$$f = \sum_{n=0}^{\infty} (f, \phi_n) \, \phi_n$$

for all square integrable functions f.

We abbreviate the integral of a square integrable function f with respect to Brownian motion by

$$N(f) = \int_{-\infty}^{\infty} f(x) \, dW_x; \tag{A.4}$$

the linear map defined by this integral is *white noise*. For all square integrable (deterministic) functions f and g, the integrals of f and g with respect to Brownian motion, W, are

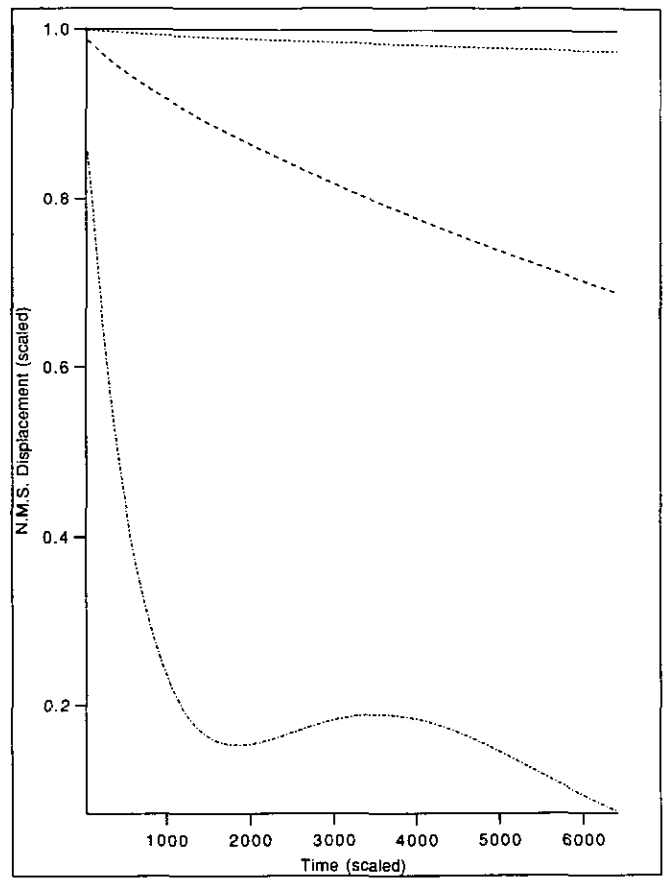

FIG. 21. Normalized mean square displacement vs time with $\bar{w} = 1$ and without stochastic error. Parameters $h = 64d$ and $d = d_0$. From top to bottom the lines indicate the results for a fields with 30, 25, 20, and 15 octaves. These graphs are normalized according to formula (5.8).

Gaussian random variables with mean and covariance given by

$$\langle N(f)\rangle = \left\langle \int_{-\infty}^{\infty} f(x)\, dW_x \right\rangle \tag{A.5a}$$

$$= \int_{-\infty}^{\infty} f(x)\langle dW_x\rangle$$

$$= 0$$

$$\langle N(f)\,\overline{N(g)}\rangle = \int_{-\infty}^{\infty} f(x)\,\overline{g(x)}\, dx \tag{A.5b}$$

$$= (f, g).$$

Property (A.5a) reflects the fact that Brownian motion has mean 0. Property (A.5b) relates the inner product for finite variance random variables to the inner product for square integrable functions. These properties characterize integration with respect to Brownian motion, just as the first and second moments of a Gaussian random variable determine its distribution.

To represent $v(\cdot)$, we must represent white noise. The moment properties of white noise allow an expansion of this process in terms of the orthonormal basis $\{\phi_n | n = 0, 1, 2, \ldots\}$, for $L^2(R)$, the square integrable functions; such an expansion is essential to the method we will

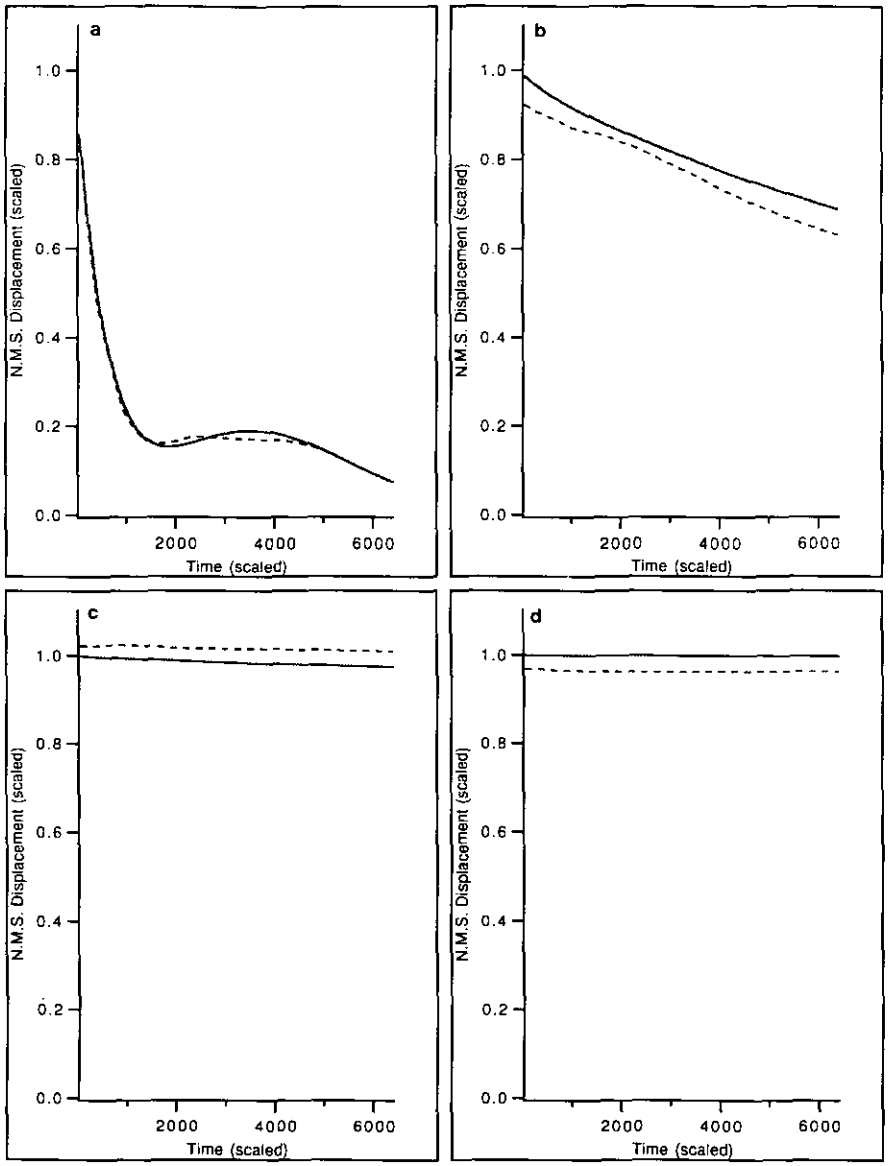

FIG. 22. Normalized mean square displacement vs time with $\bar{w} = 1$. The graphs compare the analytic values (solid line) to those simulated with 1000 realizations (dotted line) for fields with (a) 15 octaves, (b) 20 octaves, (c) 25 octaves, and (d) 30 octaves. (Other parameters and normalization are the same as in Fig. 21.)

develop. Every square integrable function f can be expanded in terms of this basis,

$$f = \sum_{n=0}^{\infty} (f, \phi_n)\, \phi_n; \tag{A.6}$$

therefore, the value of white noise on f can be similarly expanded:

$$N(f) = N\left(\sum_{n=0}^{\infty} (f, \phi_n)\, \phi_n \right)$$

$$= \sum_{n=0}^{\infty} (f, \phi_n)\, N(\phi_n)$$

$$(G * \phi_{0n}^{\sigma\tau})(x) = K \int_{-\infty}^{\infty} |y - x|^{\lambda}\, \phi^{\sigma\tau}(y - n)\, dy$$

$$= K \int_{-\infty}^{\infty} |y - (x - \lfloor x \rfloor)^{\lambda}\, \phi^{\sigma\tau}$$

$$\times (y - (n - \lfloor x \rfloor))\, dy, \tag{B.1}$$

where $\lfloor x \rfloor$ is the largest integer less than or equal to x. We shall see that the magnitude of the convolution is less than $|K|\ |n - \lfloor x \rfloor|^{\lambda - \tau}$ (for $|n - \lfloor x \rfloor|$ greater than or equal to 4).

If x is in $[0, 1)$ but not in $[n, n+1]$, then the convolution has an asymptotic expansion derived from the binomial series for the kernel. Let $C(\ ,\ )$ be the binomial coefficient

LEMMA (Far-field expansion). *If x is not in $[n, n+1]$, then*

$$(G * \phi_{0n}^{\sigma\tau})(x)$$

$$= K \int_{-\infty}^{\infty} |x-y|^{\lambda} \phi^{\sigma\tau}(y-n)\, dy$$

$$= \begin{cases} K \sum_{q=0}^{\infty} C(\lambda, q)(-1)^q M_q^{\sigma\tau} \\ \quad \times ((x - \lfloor x \rfloor) + |n - \lfloor x \rfloor|)^{\lambda - q}, \quad n - \lfloor x \rfloor \leqslant -1 \\ K(-1)^{\tau+\sigma} \sum_{q=0}^{\infty} C(\lambda, q)(-1)^q M_q^{\sigma\tau} \\ \quad \times ((1 + \lfloor x \rfloor - x) + n| - \lfloor x \rfloor|)^{\lambda - q}, \quad n - \lfloor x \rfloor \geqslant +1. \end{cases} \tag{B.5}$$

The expansion (B.5) provides an accurate means of computing convolutions when $|\lfloor x \rfloor - n|$ is large, as we discuss in Section 4B. Moreover, this far-field expansion also leads to an estimate of the decay of the convolution with distance. In turn, the decay estimate then gives a sharp estimate of the statistical energy in the tails of the multiwavelet expansion at each scale.

THEOREM. *Provided that* $|\lambda| \leqslant 1$, $\tau \geqslant 1$, *and* $|n - \lfloor x \rfloor| \geqslant 4$,

$$|(G * \phi_{0n}^{\sigma\tau})(x)| \leqslant |K|\, |n - \lfloor x \rfloor|^{\lambda - \tau}. \tag{B.6}$$

Proof. The proof follows from an application of the triangle inequality, repeated use of Holder's inequality, and the summation formula for the geometric series as follows:

$$\begin{aligned} |(G * \phi_{0n}^{\sigma\tau})(x)| &\leqslant |K| \sum_{q=\tau}^{\infty} |C(\lambda, q)\, M_q^{\sigma\tau}|\, |n - \lfloor x \rfloor|^{\lambda - q} \\ &\leqslant |K|\, |C(\lambda, \tau)| \sum_{q=\tau}^{\infty} |M_q^{\sigma\tau}|\, |n - \lfloor x \rfloor|^{\lambda - q} \\ &\leqslant |K|\, |C(\lambda, \tau)| \sum_{q=\tau}^{\infty} (q+1)^{-1/2}\, |n - \lfloor x \rfloor|^{\lambda - q} \\ &\leqslant |K|\, |C(\lambda, \tau)|\, (\tau+1)^{-1/2}\, |n - \lfloor x \rfloor|^{\lambda - \tau} \\ &\quad \times \sum_{s=0}^{\infty} |n - \lfloor x \rfloor|^{-s} \\ &= |K|\, |C(\lambda, \tau)|\, (\tau+1)^{-1/2} \frac{|n - \lfloor x \rfloor|}{|n - \lfloor x \rfloor| - 1} \\ &\quad \times |n - \lfloor x \rfloor|^{\lambda - \tau} \\ &\leqslant |K|\, |n - \lfloor x \rfloor|^{\lambda - \tau}. \end{aligned}$$

From (B.6) we obtain the important

COROLLARY (Energy criterion). *The energy at the unit scale for wavelet translates at a distance greater than or equal to r from x is*

$$\begin{aligned} E_r &= K^2 \sum_{|n - \lfloor x \rfloor| \geqslant r} ((G * \phi_{0n}^{\sigma\tau})(x))^2 \\ &\leqslant 2K^2 \frac{(r-1)^{2(\lambda - \tau) + 1}}{2(\tau - \lambda) - 1} \end{aligned} \tag{B.7}$$

for $r \geqslant 4$.

Proof. We recall the estimate

$$\sum_{n=n_0}^{\infty} n^{\alpha} \leqslant \int_{n_0 - 1}^{\infty} s^{\alpha}\, ds = -\frac{(n_0 - 1)^{\alpha+1}}{\alpha + 1} \tag{B.8}$$

for any real number α less than -1 and any integer n_0 greater than 1. (The sum is a lower Riemann sum for the integral with an integration step size of 1.) Using formula (B.6) and formula (B.8) (with $n_0 = r$ and $\alpha = 2(\lambda - \tau)$) in formula (B.7), we see that

$$\begin{aligned} E_r &\leqslant K^2 \sum_{|n - \lfloor x \rfloor| \geqslant r} (|n - \lfloor x \rfloor|^{\lambda - \tau})^2 \\ &= 2K^2 \sum_{m=r}^{\infty} m^{2(\lambda - \tau)} \\ &= 2K^2 \frac{(r-1)^{2(\lambda - \tau) + 1}}{2(\tau - \lambda) - 1}. \end{aligned}$$

Since $\lambda = (\varepsilon - 3)/2$, this implies that

$$E_r \leqslant 2K^2 \frac{(r-1)^{\varepsilon - 2(\tau+1)}}{2(\tau+1) - \varepsilon}. \tag{B.9}$$

Therefore, for $2 < \varepsilon < 4$, the sum is convergent for $\tau \geqslant 1$.

REFERENCES

1. M. Lesieur, *Turbulence in Fluids* (Kluwer Academic, Boston, 1990).
2. W. McComb, *The Physics of Fluid Turbulence* (Clarendon Press, Oxford, 1990).
3. G. Csanady, *Turbulent Diffusion in the Environment* (Geophysics and Astrophysics Monographs, Reidel, Dordrecht, 1973).
4. G. Dagan, *Annu. Rev. Fluid Mech.* **19**, 183 (1987).
5. M. Avellaneda and A. Majda, Simple examples with features of renormalization for turbulent transport *Philos. Trans. R. Soc. Ser. A* Jan. (1994).
6. M. Avellaneda and A. Majda, *Commun. Math. Phys.* **131**, 381 (1990).
7. M. Avellaneda and A. Majda, *Commun. Math. Phys.* **146**, 139 (1992).
8. M. Avellaneda and A. Majda, *Phys. Fluids A* **4**, 41 (1992).
9. A. Majda, *J. Stat. Phys.* **73**, 515 (1993).
10. D. Horntrop and A. Majda, *J. Math. Sci. Univ. Tokyo*, to appear.

11. D. Horntrop and A. Majda, Monte Carlo methods for turbulent diffusion in simple models with many spatial scales, *J. Stat. Phys.*, to be submitted.
12. A. Majda, *J. Stat. Phys.*, to appear.
13. F. Elliott and A. Majda, in preparation.
14. J. Doob, *Stochastic Processess* (Wiley, New York, 1953).
15. E. Vanmarcke, *Random Fields: Analysis and Synthesis* (MIT Press, Cambridge, MA, 1983).
16. G. Beylkin, R. Coifman, and V. Rokhlin, "Wavelets in Numerical Analysis," in *Wavelets and Their Applications*, edited by Ruskai, Beylkin, Coifman, Daubechies, Mallat, Mayer, and Raphael (Jones & Bartlett, Boston, 1992), p. 181.
17. B. Alpert, "Construction of Simple Multi-scale Bases for Fast Matrix Operations," in *Wavelets and Their Applications*, edited by Ruskai, Beylkin, Coifman, Daubechies, Mallat, Meyer, and Raphael (Jones & Bartlett, Boston, 1992), p. 211.
18. B. Alpert, Ph.D. thesis, Department of Computer Science, Yale University, December 1990.
19. I. Daubechies, *Ten Lectures on Wavelets* (SIAM, Philadelphia, 1992).
20. J. Viecelli and E. Canfield, *J. Comput. Phys.* **95**, 29 (1991).
21. R. Kraichnan, *Phys. Fluids* **13**, 22 (1970).
22. O. Kurbanmuradov and K. Sabelfeld, *Sov. J. Numer. Anal. Math. Modelling* **4**, 53 (1989).
23. K. Sabelfeld, *Monte Carlo Methods* (Springer-Verlag, New York, 1991).
24. A. McCoy, Ph.D. thesis, Department of Mathematics, University of California at Berkeley, 1975.
25. F. Furtado, J. Glimm, W. Lindquist, and F. Pereira, "Multi-length Scale Computations of Mixing Length Growth in Tracer Floods, in *Proceedings, Emerging Technologies Conference*, edited by F. Kovarik (Institute for Improved Oil Recovery, University of Houston, 1190), p. 251.
26. L. Richardson, *Proc. R. Soc. London Ser. A* **110**, 709 (1926).
27. Y. Prohorov and Y. Rozanov, *Probability Theory* (Springer-Verlag, New York, 1969).